Establishing Fluid Dynamics Scales Critical to Dynamic Interface Applications and their Impact on Handling Qualities

Quarterly Status Report 5

Period of Performance: 3/5/2022 – 6/4/2022

Prepared by:

G. R. Whitehouse
Continuum Dynamics, Inc.
34 Lexington Avenue
Ewing, NJ 08618-2302

Prepared for:

David Gonzalez
Office of Naval Research
875 North Randolph
Street
Arlington VA 22203

Under Contract No. N00014-21-C-1044

Glen R. Whitehouse

June 6, 2022

Project Summary

One of the most demanding tasks for naval aviators is landing on a moving flight deck in high sea-states (i.e. the dynamic interface (DI) problem - see Figure 1). This task is made even more difficult by aerodynamic disturbances at the landing spot from the flow around the ship's bow, superstructure and deck edges. This highly unsteady ship airwake can lead to significant pilot workload. Flight simulation has long been recognized as a valuable tool for augmenting engineering development and pilot training in DI operations, however, it is most effective when the underlying simulation model has appropriately characterized the complex aerodynamic interactions between the rotorcraft and ship airwake. Given the complexity of the problem, a fundamental difficulty when assessing the simulation approaches is the quantification of "good enough", both from the standpoint of understanding and predicting the underlying physics and also with regards to trainer fidelity (i.e. can the pilot feel/tell a difference). The premise of the proposed effort is to quantify "good enough" with regards to understanding the fundamental aero-physics of a rotorcraft interacting with an external disturbance field to quantify which length and time scales - such as those present in a ship airwake or in the wake of a an upstream aircraft during formation flight/refueling - directly impact the aircraft's fundamental response and flying qualities (FQ) along with the aeromechanics modeling fidelity required to simulate interactions adequately.

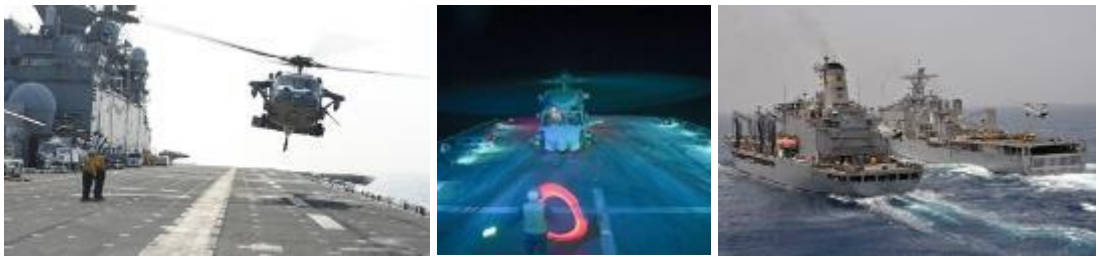

Figure 1: DI scenarios: landing on a moving deck (left), night operations (center) and approaching a pair ships (right)

Several ONR funded efforts that seek to quantify "good enough" have recently completed, or are underway, at the University of Maryland, Georgia Institute of Technology and NAVAIR, where the academic researchers are focusing on understanding the response of a wing to the wake shed by canonical structures [1] and the latter (Generalized Airwake Goodness Evaluation) program seeks to represent the entire DI scenario with a variety of methods. This effort does not seek to duplicate that work, rather to complement it by focusing on several fundamental unknowns in the rotorcraft community, namely:

1. What spatial and temporal scales, present in a disturbance field, matter from Flight Dynamics (FD) and FQ standpoints? Beyond the obvious constraints (i.e. larger than a rotor radius and those that induce velocities larger than the wake induced velocity), how does a rotor respond to different size disturbances and how does the rotor type influence this? For example, in general, a rotor acts to filter the influence of a disturbance field, but the level of filtering will vary significantly between an articulated flexible rotor (H-60) and a gimballed stiff one (V-22). Moreover, rotors typically respond ~90^o out of phase of the disturbance, whereas fixed aerodynamic surfaces response directly in-phase, which results in a fundamentally different response between rotorcraft types (i.e. helicopter vs. tiltrotor).

2. How do these scales vary when the effects on the full aircraft are accounted for? The primary response from the helicopter will be dominated by that of the rotor, though there may still be significant response associated with the disturbance induced flow on the fuselage, empennage and tail rotor.
3. How do these scales vary with aircraft configuration/type (i.e. conventional helicopter vs. tiltrotor)? The primary response from the helicopter will be dominated by that of the rotor, whereas the tiltrotor may respond primarily in a fixed wing manner associated with the induced flow on the wing. Of course, the tiltrotor's response will also vary with nacelle angle, and it is well known that the V-22's response to wake disturbances (i.e. during formation flight) is quite different to other rotorcraft in the Navy's inventory [2].
4. How do these scales vary with aircraft flight condition, and can valid modeling simplifications be made (i.e. distorting vs. classical frozen disturbance field)? Work by Whitehouse and Brown for helicopter rotors [3-7] suggests that for high speed flight, the traditional frozen field (superposition) assumption may be adequate, but that at the low speeds associated with DI operations, a distorting disturbance field and wake are required because the response is critically different.

Developing an understanding of fundamental aircraft aeromechanic response, FD, and FQ to the unknowns outlined above would provide great utility to the community with regards to establishing the level of modeling fidelity required to accurately simulate disturbance interactions, the level of fidelity required to be output by CFD simulation generated ship airwake databases for training scenarios, and the quantification and specification of handling qualities to types of disturbance fields that can be used to define future and ongoing training and aircraft performance requirements and specifications, such as ADS-33 [8].

Technical Objectives

The goal of the effort is to develop a fundamental understanding of the relationship between the length and time scales typically present in disturbance fields experienced by Naval aviators (i.e. ship airwakes, wing wakes etc.) and rotorcraft FD and FQ when the fully-interacting fluid dynamics of the airwake and rotor wake and flight mechanics are accounted for. With this information in hand, the engineering community would be better able to understand the relationship between aircraft type, ride quality, FD and FQ during flight conditions where disturbance fields are encountered. The community would be able to more accurately define trainer requirements, minimum experimental campaign requirements, minimum CFD modeling requirements and consequently establish a benchmark to evaluate CFD predictive capability. Furthermore, the conclusions of this work would also directly impact the development of requirements for new aircraft given the direct correlation between FD and FQ. The proposed effort would undertake the research required to develop such an understanding, with disseminating the observations and conclusions of the work to the Navy and the broader FD, FQ and handling qualities communities - a key objective from the outset. The effort will be structured using a build-up approach that first focuses on defining relevant disturbance fields followed by predicting and understanding the fundamental aeromechanics response (i.e. aerodynamic forces and moments and rotor dynamics). The effort would culminate in predicting the flight dynamics and handling qualities for realistic, but generic, helicopter and tiltrotor configurations that include representations of flight controls, propulsion system and cross-

coupling characteristics. The key objectives for the effort roughly form the main tasks and are as follows:

1. Define the spatial and temporal fluid dynamic scales present in relevant disturbance fields and develop numerical representations for testing (Year 1).
2. 6-DOF generic model assembly and shakedown testing to ensure correct operation and functionality.(Year 1)
3. Define aeromechanics performance and HQ metrics along with a detailed simulation test matrix that includes systematic and consistent model fidelity build-up (Year 1-2).
4. Undertake simulation of a generic helicopter interacting with frozen and distorting disturbance fields to establish fundamental response characteristics (Year 2).
5. Undertake simulation of a generic tiltrotor interacting with frozen and distorting disturbance fields to establish fundamental response characteristics (Year 2).
6. Develop a realistic full helicopter model and undertake simulations of interactions with frozen and distorting disturbance fields to establish flight dynamics and handling qualities response (Year 3).
7. Develop a realistic full tiltrotor model and undertake simulations of interactions with frozen and distorting disturbance fields to establish flight dynamics and handling qualities response (Year 3).
8. Documentation and dissemination of observations and conclusions to the Navy and the wider FD/HQ community (Years 1-3).

Summary of Work Conducted During Reporting Period

During this progress period, work has continued on the development and testing of the method for formulating canonical airwake presented in the previous progress report. This method employs time-accurate flow simulations of flow over a cube as a starting point and entails fitting analytical vortex models are primary flow features observed in the simulation results, and subsequently superimposing these models to reconstruct the airwake velocities. Such an approach has the potential to capture flow dynamics relevant to flight dynamics and handling qualities, and paves the way for parametrization and scaling, such that the airwake generated in the vicinity of differing ship geometries and/or varying freestream velocities may be adequately represented by modifying the inputs to the vortex models, without having to carry out explicit CFD calculations for every single ship configuration. The approach is currently under investigation and additional results are provided in this report. Note that the work presented here builds upon early work performed under a concurrent effort for NASA (Contract No. 80NSSC21C0026) that aims to develop a ride quality assessment tool for urban air mobility (UAM) aircraft. Features considered during the present progress period are appended to results presented in the previous progress report to maintain continuity.

During this performance period CDI obtained permission to access and use the Navy's CASTLE simulation environment. We are currently awaiting formal access to the software from engineers at NAVAIR's Manned Flight Simulator

Simplified Wake Representation

CFD Simulation and Validation

CFD simulations were undertaken of the flow around a cube in order to develop a dataset against which to compare analytical models. Flow over cube was chosen as it represents a minimum complexity canonical obstacle, and simulation results were compared to those from literature for validation. CFD predictions were performed using the CDI CGE/VorTran-M flow solver [9-11]. CDI's adaptive cut-cell octree Cartesian Grid solver (CGE) solves the compressible URANS equations using either a Spalart-Allmaras (SA and SA DES) or a shear stress transport (SST) turbulence models. Modern turbulence specific adaptive wall functions are available in CGE in order to efficiently represent the flow in boundary layers. Resolving the evolution of vortical structures, such as those shed from bluff bodies, can be particularly expensive in primitive variable CFD solvers; therefore, CGE is coupled to the VorTran-M vorticity-velocity solver in order to reduce computational costs. The CGE/VorTran-M coupling arrangement consists of implementing the CGE solution on the grid as an "inner" solver that extends sufficiently far to contain regions with significant compressibility or flow turbulence and VorTran-M as an "outer" solver that is applied in the essentially incompressible flow region and efficiently transports and evolves the vorticity with minimal dissipation. Such an arrangement allows for computational savings in mesh resolution of several orders of magnitude when compared to pure CGE simulations.

Primary flow features associated with a headwind flow over a cube are illustrated in Figure 2, and include

- A horseshoe vortex that forms upstream of the obstacle where the flow stagnates and wraps around the cube (feature "A" on the figure);
- On the top and side surfaces, local separation and reattachment regions ("B" and "C" on the figure);
- In the lee of the obstacle, an arch vortex (feature "D" on the figure) forms due to the separation of the shear layers from the top and side surfaces. The streamlines aft of the obstacle indicate a recirculation region, where the direction of the flow reverses.

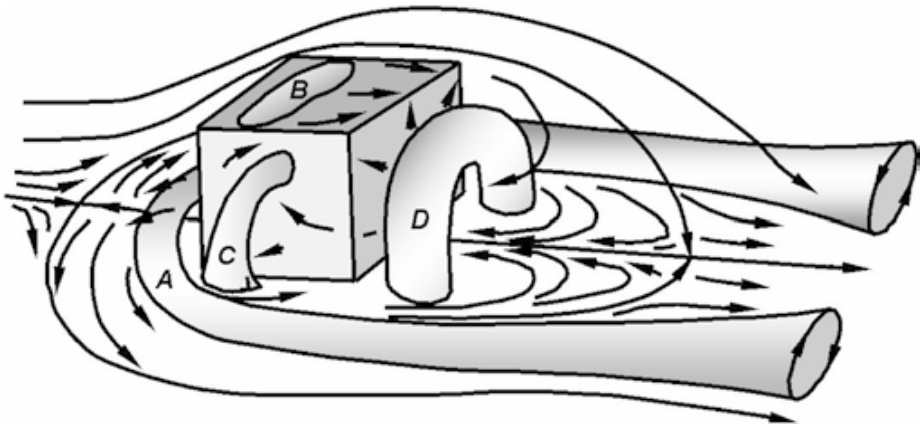

Figure 2: Schematic of principal flow features around surface-mounted obstacle [12].

CGE/VorTran-M simulations were performed for a 30 m/s headwind simulation over a 10 m cube. Although this speed is larger than would be typically encountered in practice, it is necessary to use a larger freestream velocity to maintain good numerical conditioning of the

compressible flow solver. An alternative approach would have been to take advantage of the preconditioners implemented in CGE for low-speed flows, however, we deemed using the higher velocity appropriate given that the flow field is dominated by separation from the sharp edges of the cube, which has a weak dependence on viscosity. This further allowed us to perform simulations for inviscid flow only as in [9] since neglecting viscosity effects allows for scaling of time-accurate flow predictions using freestream velocity. Note that no explicit atmospheric boundary layer (ABL) model was included in the simulation, though this option is available. Simulations were performed using a fixed time step of 0.005 seconds, and, after washing out the initial conditions, a transient simulation was of 25 seconds was undertaken. Results were post-processed based on the last 22 seconds of the simulations. The first three seconds of the prediction were removed in case there were any residual non-physical transient effects.

Vortex shedding frequency is characterized by the Strouhal number, which is defined as

$$St = \frac{fb}{U}, \tag{1}$$

where f is the vortex shedding frequency and b is the characteristic length. Results from literature indicate dominant periodicity for flow aft of a cube at a distance of 6H [13] to have a characteristic frequency of $St = 0.104$ [13, 14] (compared to $St = 0.2$ for a flat plate). Using the 10 m cube length as characteristic length and the freestream velocity of 30 m/s as characteristic velocity, this Strouhal number corresponds to a vortex shedding frequency $f = 0.3$ Hz, which, in turn corresponds to a period of 3.2 seconds. The trimmed 22 second simulation duration thus allows for approximately 7 cycles of vortex shedding to be captured, with approximately 640 time steps per cycle.

The qualitative flow features described previously are captured by the CGE/VorTran-M simulations as shown in Figure 3(a) to (d). The origin of the global coordinate system shown in the figures is located at the center of the bottom face of the cube. In Figure 3(a), the separation region over the top of the cube surface and recirculation zone aft of the obstacle are evident. The velocities in the recirculation zone reach magnitudes close to 15 m/s, which is half of the freestream velocity. Figure 3(b) displays the horseshoe vortex which starts upstream of the obstacle. Longitudinal velocity contour plots along a transverse plane that passes through the center of the obstacle at $t = 4.7$s and $t = 6.7$s are shown in Figure 3(c) and 2(d), respectively. Flow separation on the sides of the obstacles is evident in these figures. An alternating vortex shedding pattern representative of the classic von Karman streak is noted as well.

Spectral analysis of longitudinal velocity and velocity magnitude were performed for three points aft of the cube to obtain a quantitative validation of the simulation. These points correspond to $z = \{H, 2H, 3H\}^T$ and $y = 0.5H$, where $H = 10$ m is the cube height. Velocity magnitude was considered to account for 3D flow effects in characterizing vortex shedding frequency. Time histories and Fourier Transform plots for longitudinal velocity and velocity magnitude are shown in Figure 4 and Figure 5, respectively. The dominant frequency in all spectral plots is 0.5 Hz. Secondary peaks are noted at 0.4 Hz in the $z = 2H$ and $z = 3H$ plots. The actual frequency is thus expected to be between 0.4 and 0.5 Hz. Using the cube length of 10 m as characteristic length, and the freestream velocity of 30 m/s as characteristic velocity, this corresponds to characteristic frequency of approximately 0.15. There is thus a minor discrepancy between the Strouhal frequency obtained from the CGE/VorTran-M simulation and that from the literature, but is deemed acceptable for the current investigation which is focused on phenomenology and developing simplified representations.

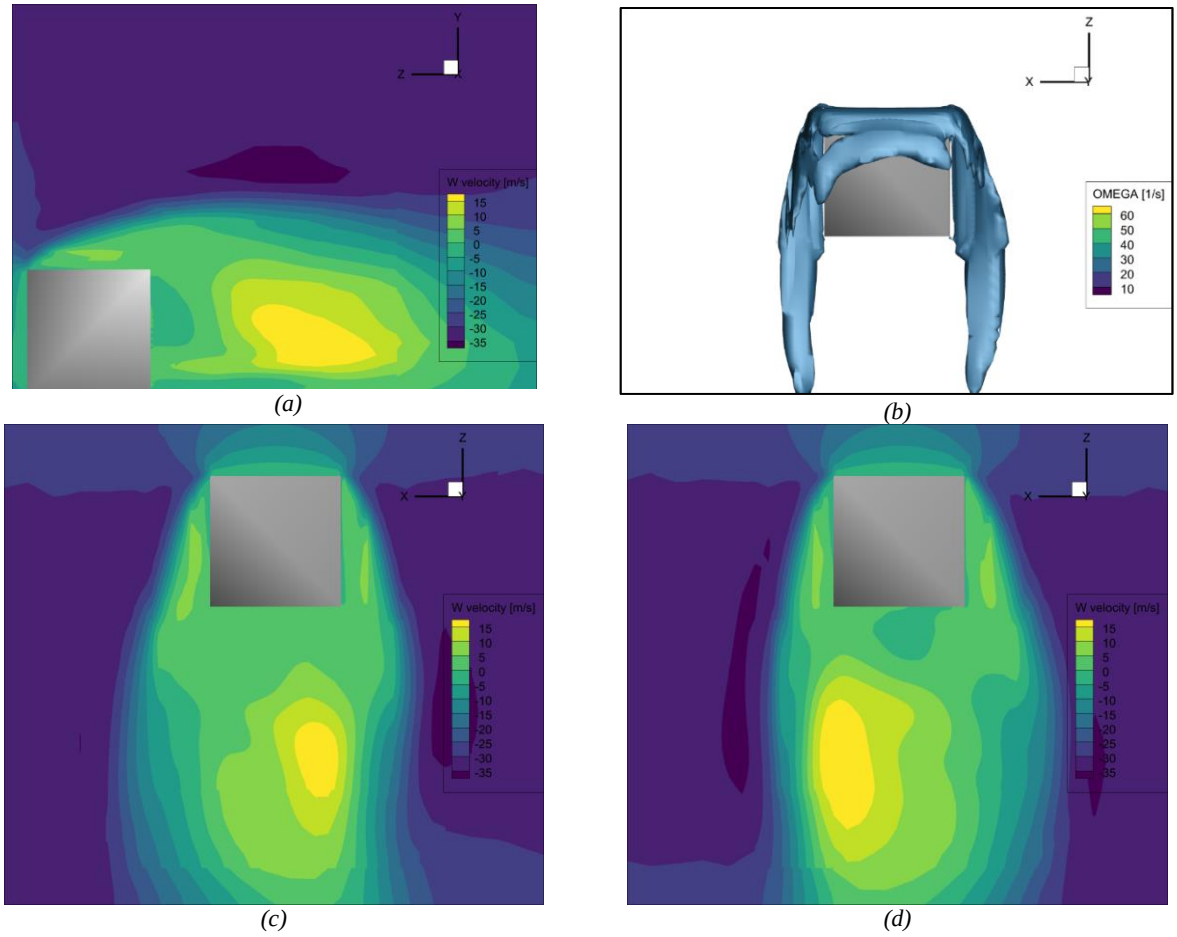

Figure 3: Flow features associated with a 30 m/s headwind flow simulation over a 10m cube using CGE/VorTran-M: (a) contour of longitudinal velocity through midplane (side view), (b) iso-surface of vorticity magnitude (top view), (c) contour of longitudinal velocity on a midplane at $\boldsymbol{t = 4.7\ s}$ *(top view) and (d) contour of longitudinal velocity on a midplane at* $\boldsymbol{t = 6.7\ s}$ *(top view).*

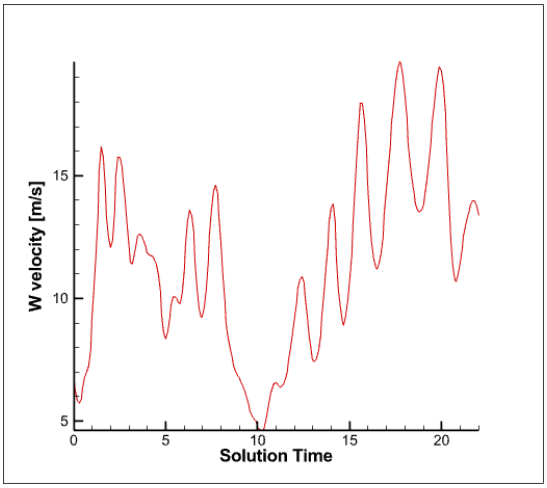

(a) $z = H$, time history

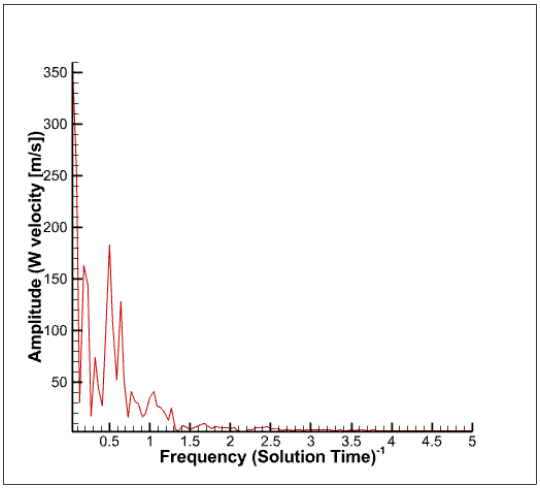

(b) $z = H$, Fourier transform

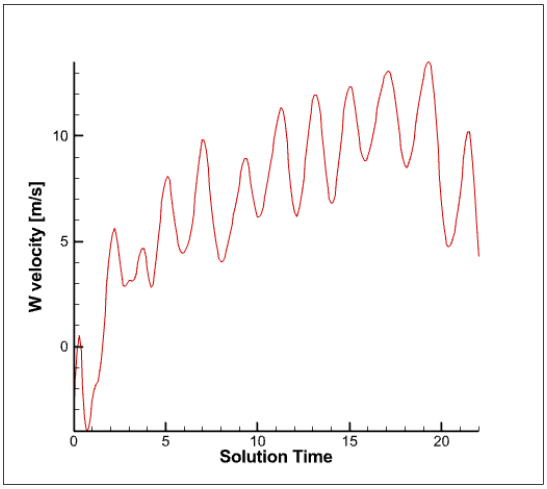

(c) $z = 2H$, time history

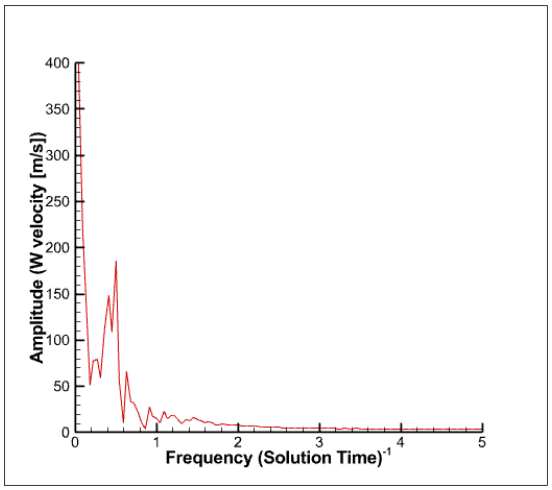

(b) $z = 2H$, Fourier transform

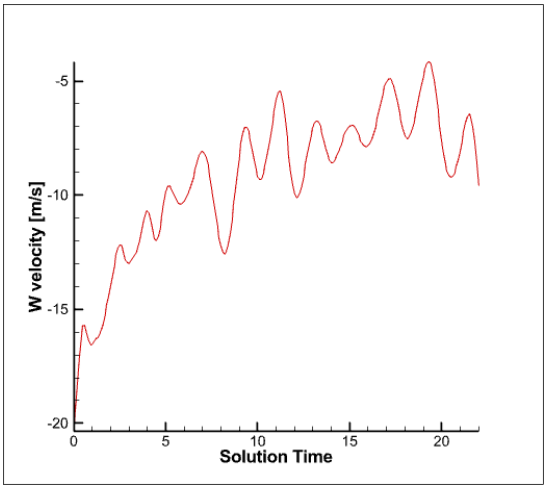

(e) $z = 3H$, time history

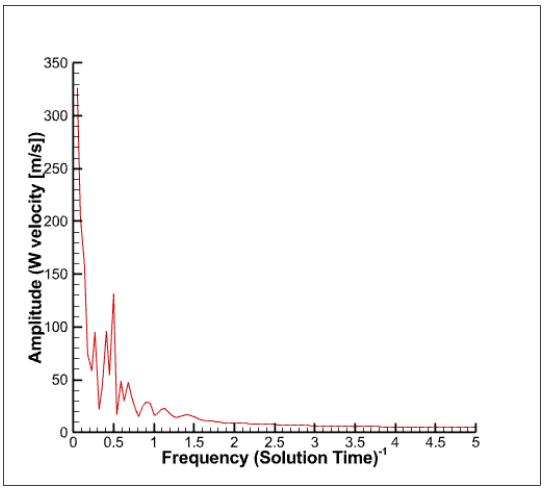

(b) $z = 3H$, Fourier transform

Figure 4: Time histories and corresponding Fourier transform plots of longitudinal velocity at points aft of the cube at $y = 0.5H$.

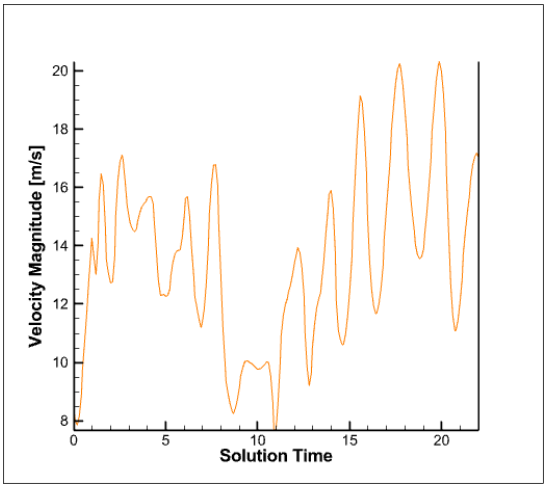

(a) $z = H$, time history

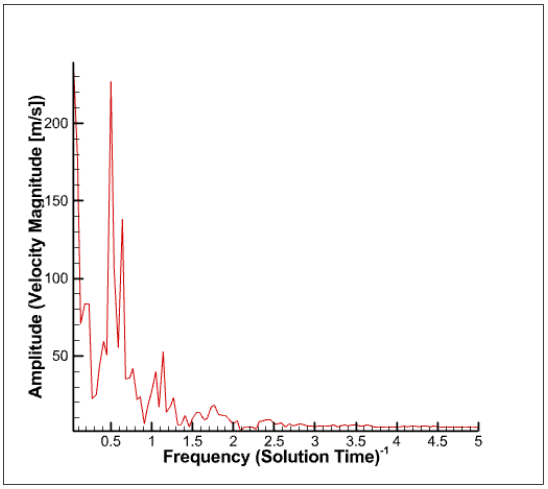

(b) $z = H$, Fourier transform

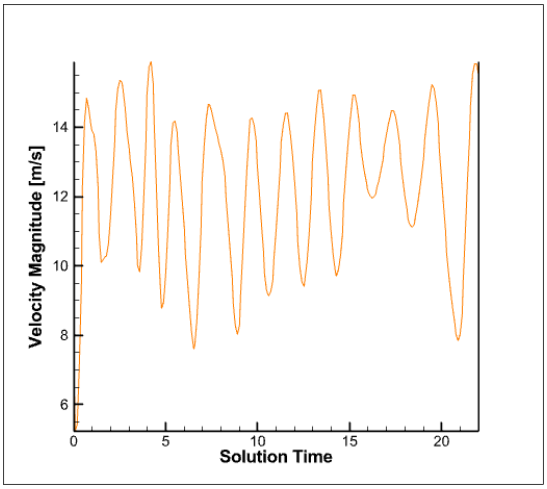

(c) $z = 2H$, time history

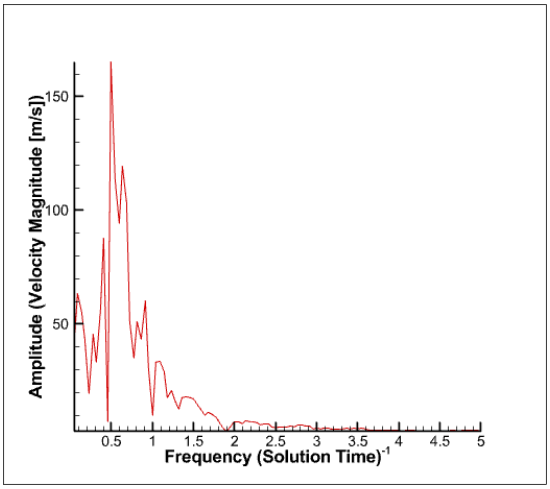

(b) $z = 2H$, Fourier transform

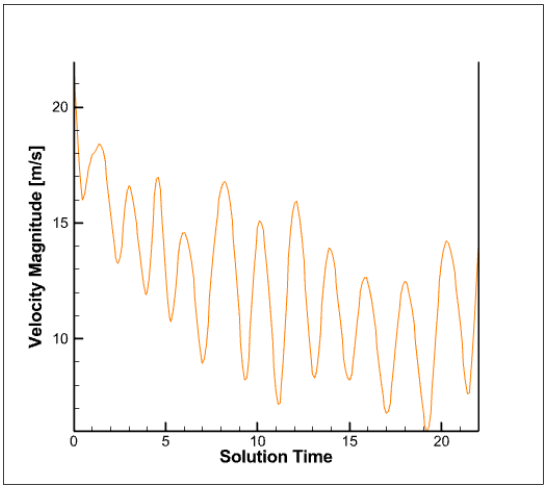

(e) $z = 3H$, time history

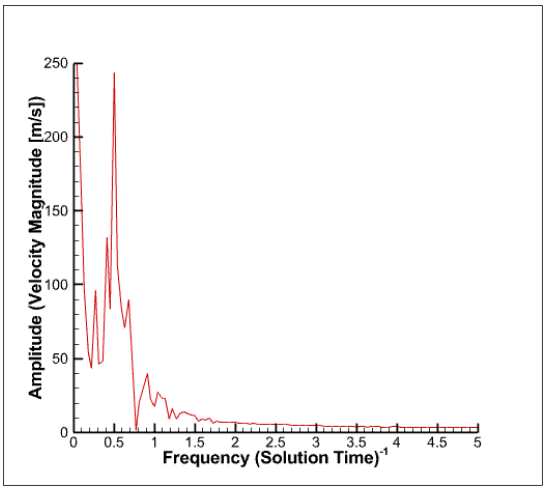

(b) $z = 3H$, Fourier transform

Figure 5: Time histories and corresponding Fourier transform plots of velocity magnitude at points aft of the cube at $y = 0.5H$.

Vortex Model Fitting

Six primary flow features were identified from the CFD simulation simulations and are shown in Figure 6. Given these vortex-based features, we investigate the development of an airwake model that would reconstruct the airwake velocities through a linear superposition of analytical vortex models that capture the velocity profile distributions associated with each of these flow features. Two-dimensional vortices are chosen as starting point for simplicity. When superimposing these vortices to generate 3D airwake profiles, proper coordinate transformations and weightings to control the influence of the individual vortices in the 3D spatial and temporal domain will have to implemented. The use of analytical vortex models paves the way for parametrization and scaling such that the airwake around different ship geometries may be obtained by modifying inputs to the vortex models, without having to carry out explicit CFD calculations. Model fitting has been performed for the top surface flow separation (Figure 6(a)), separation over the side surfaces Figure 6(b)), backward-facing step separation (Figure 6(d)) and edge vortices (Figure 6(f)). The von Karman streak illustrated in Figure 6(e) is only noted in time-accurate simulations. In time-averaged contours of velocity components, a symmetrical distribution of velocity is noted. Model fitting has been performed for this symmetrical representation as well. These are further described below.

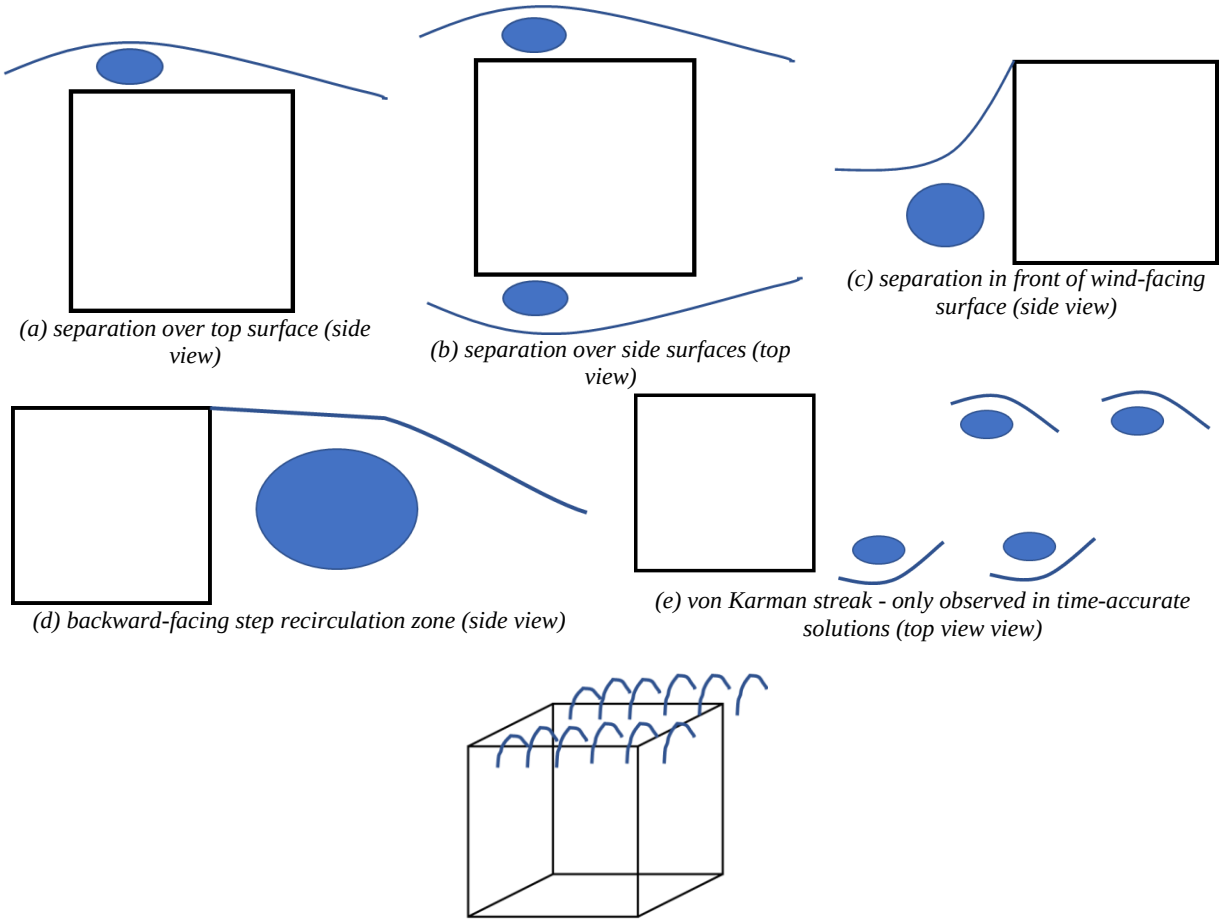

(a) separation over top surface (side view)

(b) separation over side surfaces (top view)

(c) separation in front of wind-facing surface (side view)

(d) backward-facing step recirculation zone (side view)

(e) von Karman streak - only observed in time-accurate solutions (top view view)

(f) edge vortices on top surface that develop due to pressure gradients between side and top surfaces (perspective view)

Figure 6: Primary flow features identified from CGE/VorTran-M simulation of 30 m/s headwind over 10 m cube; freestream direction from left to right.

Top-surface flow separation modeling

Flow detaches at the top edge of the wind-facing surface and reattaches in the lee of the obstacle (see. Figure 2). Due to the interaction of the incoming freestream above the obstacle with this separation, a recirculation zone is created on the top surface. The flow can also reattach on the top surface, depending on the incoming free stream speed and obstacle dimensions [15]. Recirculation zones are typically associated with a swirling velocity field, making the use of vortex models suitable. For this region, a vortex model based on the one proposed Banks and Meroney [16, 17] is used to capture the longitudinal velocity profile along the midplane of the obstacle.

This validated 2D model was developed to capture the influence of conical vortices on surface pressure. Conical vortices are generated from sharp corners in oblique wind conditions (see Figure 7). These vortices have been studied extensively by the wind engineering community given that they generate high suction regions on roofs of low-rise buildings, which, in turn, can lead to severe structural damage [18-20]. A depiction of the vortex flow model is shown in Figure 8 [16], where a vortex of radius h with center at point O is placed above the surface such that it touches the surface at point S. To allow for a smooth transition from constant

vorticity within the vortex to regions of zero vorticity where potential flow theory applies, a transition region is introduced, with point *M* on Figure 8 indicating the start of the potential flow region. Point *C* represents the location of maximum velocity in the transition region and is typically set to the midpoint location in the transition region. The vortex is envisioned to be driven like a wheel, spinning due to freestream velocity acting at point *M* [16]. Banks and Meroney provide piece-wise continuous expressions for velocity across five distinct regions of the domain, shown in Figure 9. The nondimensional coordinate $a = \zeta/h$ will be used when referencing distances relative to the vortex center. The core is assumed to have a diameter of $0.2h$ and represents a region dominated by viscosity, where flow follows a solid body rotation motion. In the region between the core and transition ($0.2 < a < 1$), the velocity profile is based on a power curve fit to the velocity profile obtained from a Navier-Stokes based simulation for a 65° swept delta-wing at a 10° angle of attack at 70% chord and Mach number $Ma = 0.85$. This relation is used because of the similarity between conical vortices on the roof of a building and delta-wing vortices observed on delta-wing aircraft. Between the core and roof surface (-1 < a < 0.2), pressure changes occur due to centrifugal accelerations of the vortex, such that the resulting governing equation is [16]

$$\frac{dP}{dn} = \frac{\rho U^2}{R_c}, \tag{2}$$

where P is the pressure, n is the unit normal to the curvature, ρ is the fluid density, U is the fluid speed in the direction of the vortex, and R_c is the radius of curvature. In the potential flow region, flow merges with freestream and both Bernoulli's equation and Eq. (2) are obeyed. The equations representing the velocity profile from this model are summarized in Table 1. There are three primary inputs to the model: (1) the vortex radius (h), (2) the location of point M (R_M), and (3) the velocity at point M (U_M).

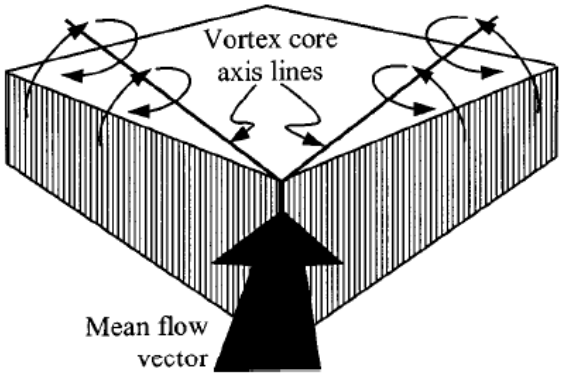

Figure 7: Illustration of conical vortices that form on roof in oblique wind conditions [16].

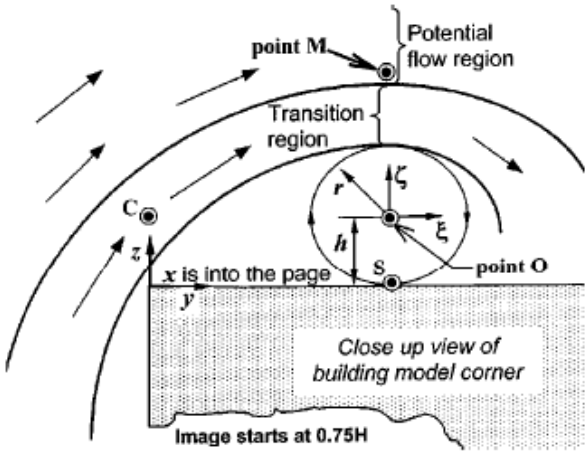

Figure 8: Illustration of the vortex model proposed by Banks and Meroney [17].

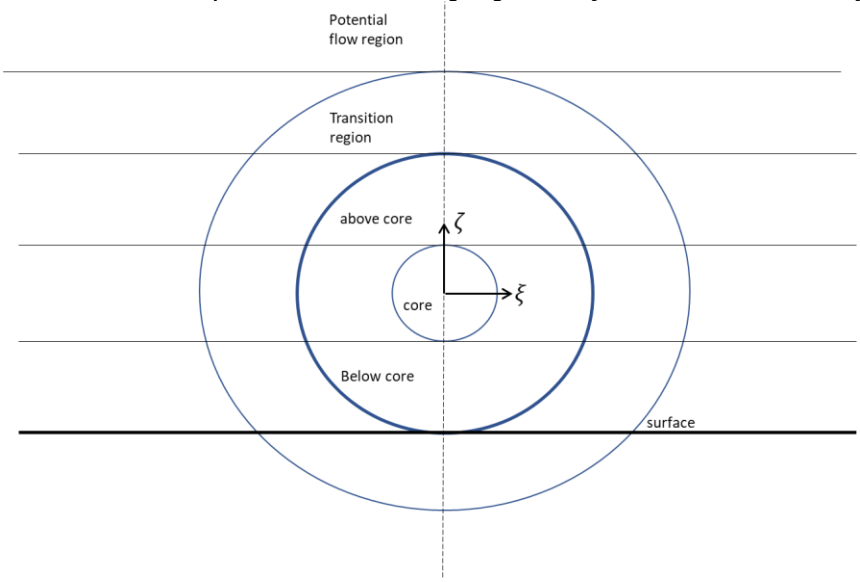

Figure 9: Illustration of the vortex model proposed by Banks and Meroney highlighting the five regions considered.

Table 1: Velocity profile equations for Banks and Meroney vortex model [16]; $a_1 = 0.2$ is used to delimit vortex core size, $a_2 = 1$ is used to delimit vortex size, a_3 is used to demark start of potential flow region, a_{max} is used to denoted the point in the transition region where maximum velocity is obtained, U_{max} is taken to be the velocity at point M, $U_{a_1} = U_{vortex}(a_1)$, $U_{a_2} = U_{transition}(a_2)$, $U_{a_3} = U_{tranistion}(a_3)$ and $n' = n/h$.

R_c/h	Range	Description	Velocity Equation
$-\infty$	$a = -1$	Roof surface	$U = 0$
$a/(1+a)$	$-a_2 < a < -a_1$	Between roof and vortex core	$U(a) = -U_{vortex}(a) = -U_{a_2} \cdot \sqrt{a/-a_2}$
a	$\lvert a \rvert < a_1$	Viscous vortex core	$U(a) = U_{core}(a) = U_{a_1} \cdot a/a_1$
$a + a^3/2$	$a_1 < a < a_2$	Vortex, above core	$U(a) = U_{vortex}(a) = U_{a_2} \cdot \sqrt{a/a_2}$
$a + a^3/2$	$a_2 < a < a_3$	Transition region	$U(a) = U_{transition}(a) = \frac{U_{max} \cdot 2 \cdot (a/a_{max})}{1 + (a/a_{max})^2}$
$a + a^3/2$	$a_3 < a$	Potential flow region	$U(a) = U_{potflow}(a) = U_{a_3}\sqrt{e^{\int_{a_3}^{a} \frac{-2}{(R_c/h)} dn'}}$

Tecplot's vortex core extraction feature was used to identify the location of the time-averaged vortex for the top separation, highlighted in Figure 10. This location corresponds to z = 2.5 m relative to the global coordinate system. Banks and Meroney's vortex model was used to determine the longitudinal velocity profile along a vertical line that passes through the identified vortex core center. The vortex radius h was determined by manual tuning to best capture the velocity profile predicted by CGE/VorTran-M. Following the approach laid out in Ref. [17], point M can be selected to be at a location where the correlation coefficient between the velocity at the given location and the surface pressure coefficient at point S is close to 1. Figure 11 shows a plot of the correlation coefficient as a function of height from the top surface, and suggests that any point above y = 3.2 m can be chosen. The location of point M was determined by manual tuning to best capture the velocity profile. The final model parameters and corresponding velocity profile are shown in Table 2 and Figure 12(a), respectively. Velocity predictions from the model closely follow those from the CGE/VorTran-M simulation, with maximum offsets of approximately 4 m/s, noted in the regions above the core center. Below the core center, model predictions deviate from CFD, which, interestingly, seem to follow a viscous boundary layer (BL) profile despite being inviscid. This appears to be due to the suction pressures associated with the separated flow over the top surface, and the deviation from CGE predictions below the vortex center is expected given the symmetry in the vortex model. The velocity profile below the vortex center can be adequately captured using a quadratic fit of the form

$$\mathrm{U(y)} = \mathrm{c_1}(-\mathrm{y}^2 - \mathrm{y}), \tag{3}$$

as shown in Figure 12(b). The constant $\mathrm{c_1} = 10$ was used to generate the figure.

Table 2: Vortex model parameter values; distances specified relative to top surface.

Parameter	Value
h (m)	1.5
R_M (m)	4.9
U_M (m/s)	-32.6

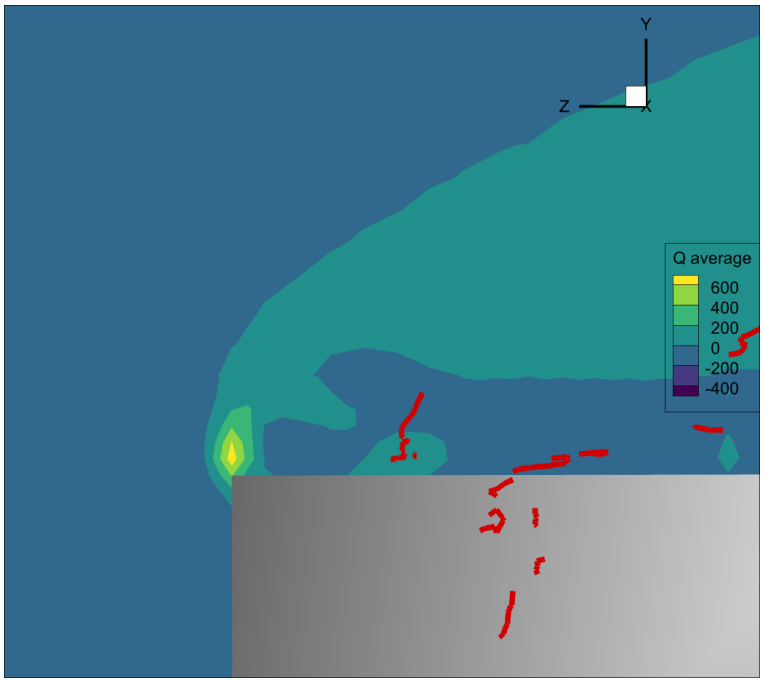

Figure 10: Contour of the time-averaged Q criterion across a midplane through the center of the obstacle; red lines indicated vortex core centers determined by Tecplot.

Steps were taken to expand the vortex model predictions from the one-dimensional vertical line across the vortex center to the full 2D region over the top surface of the cube. The equations in Table 1 are expressed in radial coordinates. However, the velocity profiles obtained using the model for radial lines at nonzero angular displacements from the vertical axis did not adequately capture results from CFD, as illustrated in Figure 13 where velocity profiles for radial lines at $\theta = 30°$ and $\theta = 60°$ (with θ measured counterclockwise from the ζ axis in Figure 9) are plotted.

An alternate method to obtain the 2D velocity profile was thus devised. Vortex model fitting was performed at five different span locations along the top surface of the cube; $z = \{5, 2.5, 0, -2.5, 5\}$ m, resulting in five corresponding values for the model inputs h, R_M and U_M, summarized in Table 3. The velocity profile prediction for $z = -2.5$m is shown in Figure 12 whereas the other four locations are shown in Figure 14. Except for the region within a height of 1m from the top surface at z = 5m (Figure 14(a)), the manually tuned vortex models at the various span locations show reasonable agreement with CFD predictions. The $z = 5$m location corresponds to the leading-edge corner of the top vortex. The discrepancy within the 1m region from the surface is acceptable given that in practice, the aircraft will be very close to landing at that position, and it's unlikely that velocities at this height will have any influence on flying qualities. Furthermore, if this height is nondimensionalized by the cube height $H = 10$m, we can generalize that model predictions are likely not valid in the $0.1H$ region above the obstacle

near the leading edge. Maximum offset at the $z = 5$m span location is noted in the potential flow region, where deviations of approximately 20% from the -30 m/s predicted by CGE/VorTran-M are evident. These deviations are also considered to be acceptable in the current study.

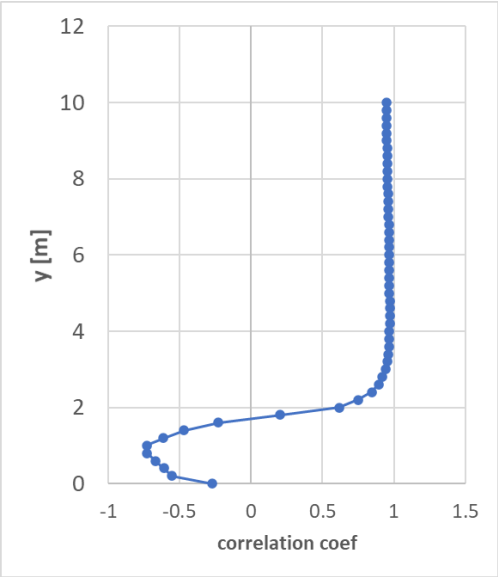

Figure 11: Correlation coefficient between longitudinal velocity at various heights above the top surface and surface pressure.

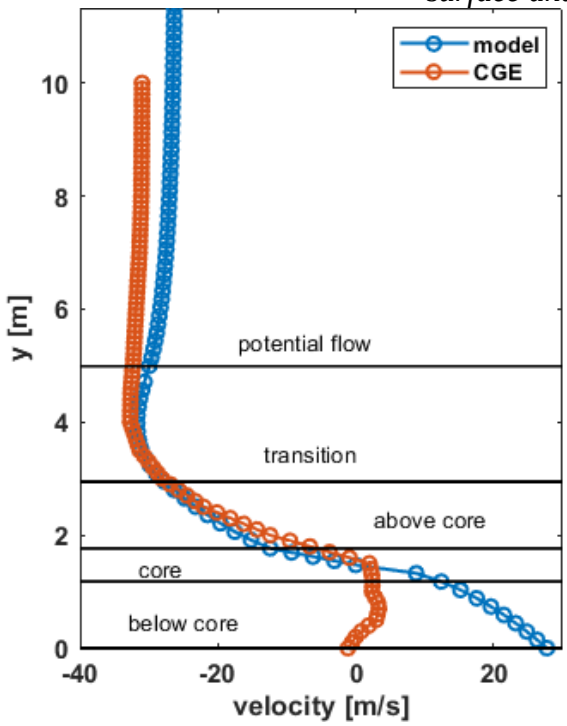

(a) original vortex model equations used

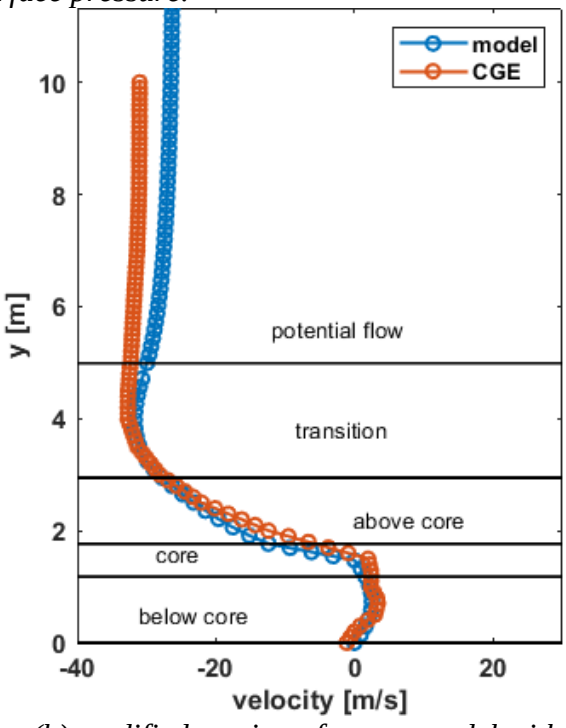

(b) modified version of vortex model with quadratic fit below vortex core center used

Figure 12: Velocity profile along vertical line at $\boldsymbol{z = 2.5}$*m.*

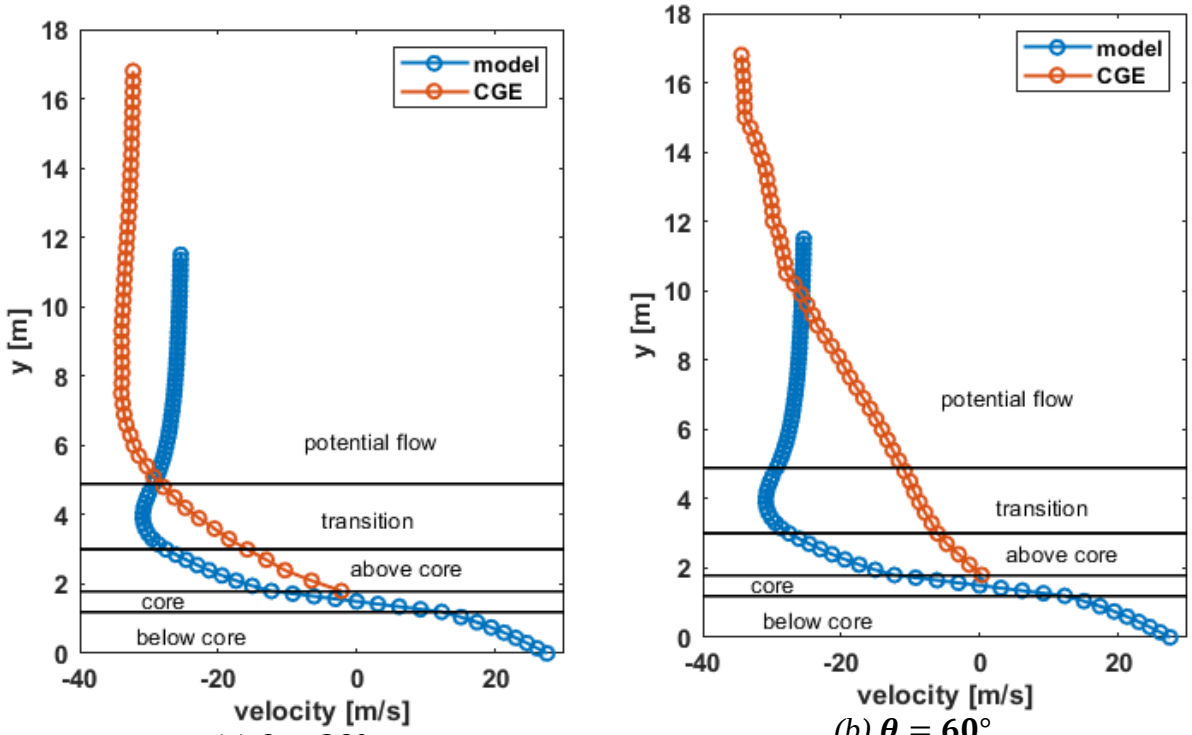

(a) $\boldsymbol{\theta = 30°}$ *(b)* $\boldsymbol{\theta = 60°}$

Figure 13: Velocity profile along non-vertical radial line with vortex center at $\boldsymbol{z = 2.5}$*m.*

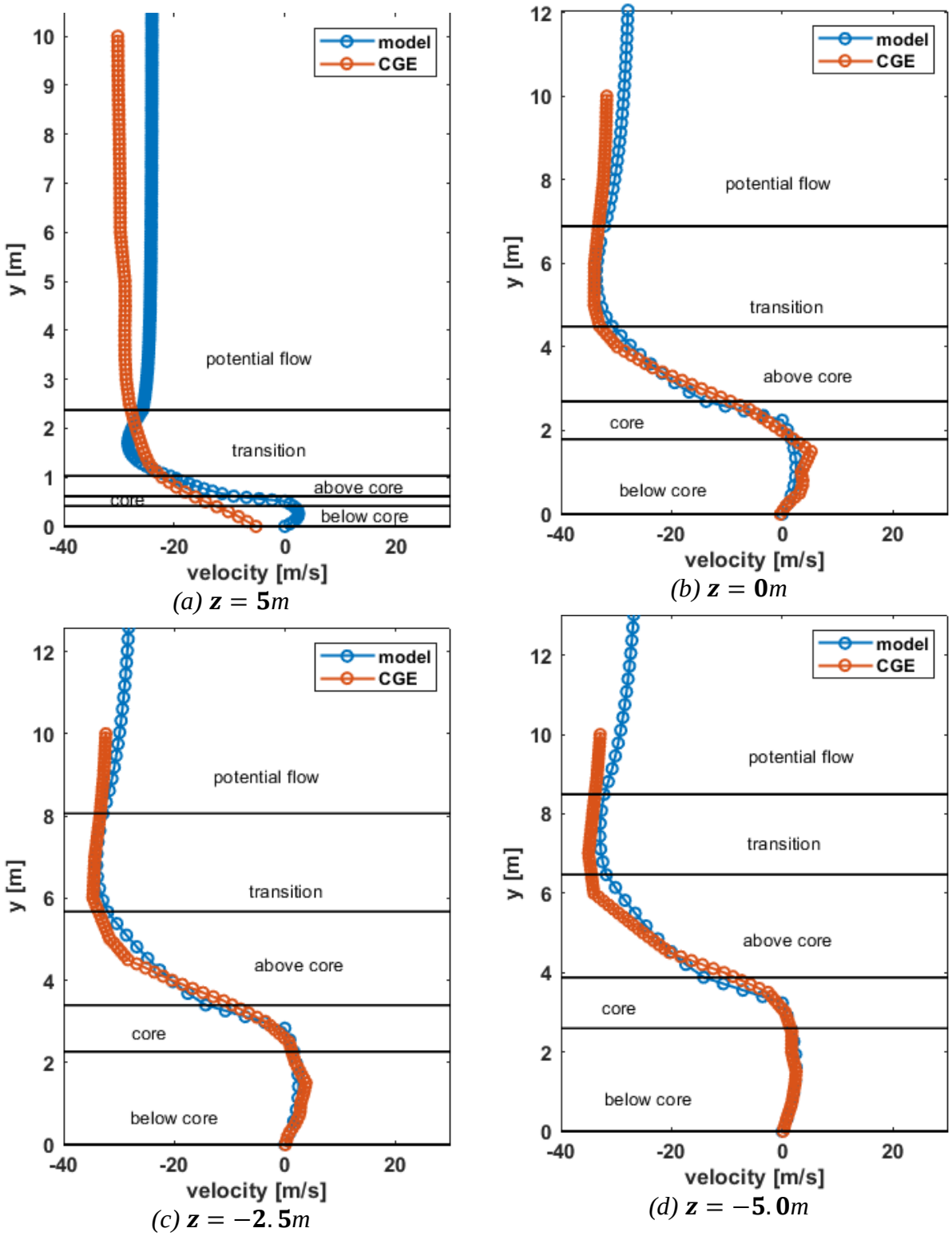

(a) $z = 5m$ (b) $z = 0m$

(c) $z = -2.5m$ (d) $z = -5.0m$

Figure 14: Velocity profile at various longitudinal span locations for a 30 m/s headwind.

Table 3: Vortex model input parameters for various longitudinal span locations.

z [m]	h [m]	U_M [m/s]	R_M [m]
5	0.5	-28.0	2.4
2.5	1.5	-32.6	4.9
0	2.25	-33.2	7.0
-2.5	2.8	-33.6	8.0
-5	3.25	-33.2	8.5

Quadratic polynomials were fitted onto the values in Table 3 to obtain spanwise functions $h(z), R_M(z)$ and $U_M(z)$. The resulting equations are valid over the top surface of the cube ($-5 \leq z \leq 5$ m). Velocity profile predictions at $z = \{3.5, -3.5\}$ m are plotted in Figure 15. These locations were not considered during the fitting but still show good agreement with predictions from CFD.

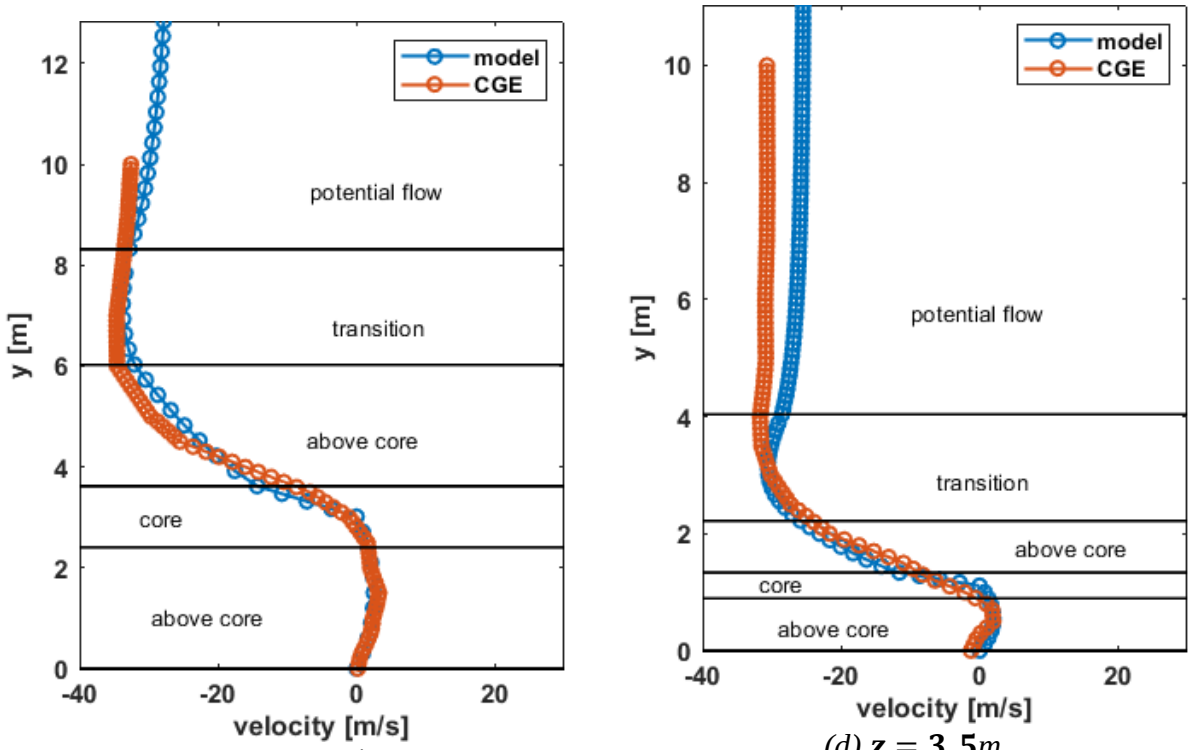

(c) $\boldsymbol{z = -3.5m}$ *(d)* $\boldsymbol{z = 3.5m}$

Figure 15: Velocity profile at two longitudinal span locations not used in determining $\boldsymbol{h(z), R_M(z)}$ *and* $\boldsymbol{U_M(z)}$.

The 2D vortex model used to capture the velocity profile along the top surface of the cube is effectively an extension of the Banks and Merony model [16, 17] that assumes an infinite number of overlapping vortices of differing sizes exist along the top surface. This representation adequately captures the velocity profile for the current case study where flow reattaches in the lee of the obstacle. For flow regimes where reattachment occurs on the top surface directly, modifications to this model may be required.

A preliminary model scaling investigation was also carried out using CGE/VorTran-M simulations of a 40 m/s headwind over the cube. It was found that the velocity profile along the top surface of the cube along the midplane could be captured by the model by simply scaling $U_M(z)$ for the 30 m/s case accordingly, see Figure 16. As noted previously, this scaling relationship is expected given the inviscid solver being used but also is a good approximation when viscous flow effects are included given the magnitude of the operating Reynolds number.

The application limits of the vortex model presented above still need to be investigated but we anticipate it to be applicable to rectangular prisms of varying dimensions. Model input parameters h and R_M can be potentially parametrized for scaling using either the height, length, or width of the obstacle, and the rotational velocity U_M using freestream velocity.

Backward-facing step flow separation modeling

Aft of the cube, shear layers are shed from the top and side edges of the backward-facing surface, see Figure 2. The shear layers shed from the top edge are considered here (Figure 6(d)), and vortex model fitting is currently being performed using time-averaged longitudinal velocity profiles aft of the obstacle. In practice, vortex shedding in this region is dynamic; the location where the shear layer impinges on the wall fluctuates, shifting the reattachment zone upstream and downstream in a low frequency motion [21-24], with the recirculation bubble shrinking and expanding accordingly. We plan to account for these dynamics once vortex models that adequately capture time-averaged velocity profiles have been obtained.

Time-averaged streamlines across the midplane of the cube are shown in Figure 17, and a single leeside primary vortex structure is evident. The center of the vortex was found to be at $(z, y) = (-18.8, 10.9)$ m using Tecplot's vortex core extraction feature.

Vortex model fitting was performed to capture the longitudinal velocity profile along a vertical line through the identified vortex center. Peak longitudinal velocity of 14.7 m/s was noted at $y = 2.9$ m along that line. A Rankine vortex model was first used with a velocity profile given by

$$U(y) = \begin{cases} \Omega r & r \le r_c \\ \dfrac{\Omega r_c^2}{r} & r > r_c \end{cases}, \tag{4}$$

where Ω is the angular rotation speed of the vortex, determined using the peak longitudinal velocity and vortex core radius r_c (set here to 8 m, which is the distance from the vortex center to the location where peak longitudinal velocity is noted). As evident in Figure 18, the linear velocity variation associated with the Rankine vortex core failed to adequately represent the velocity profile predicted by CGE/VorTran-M.

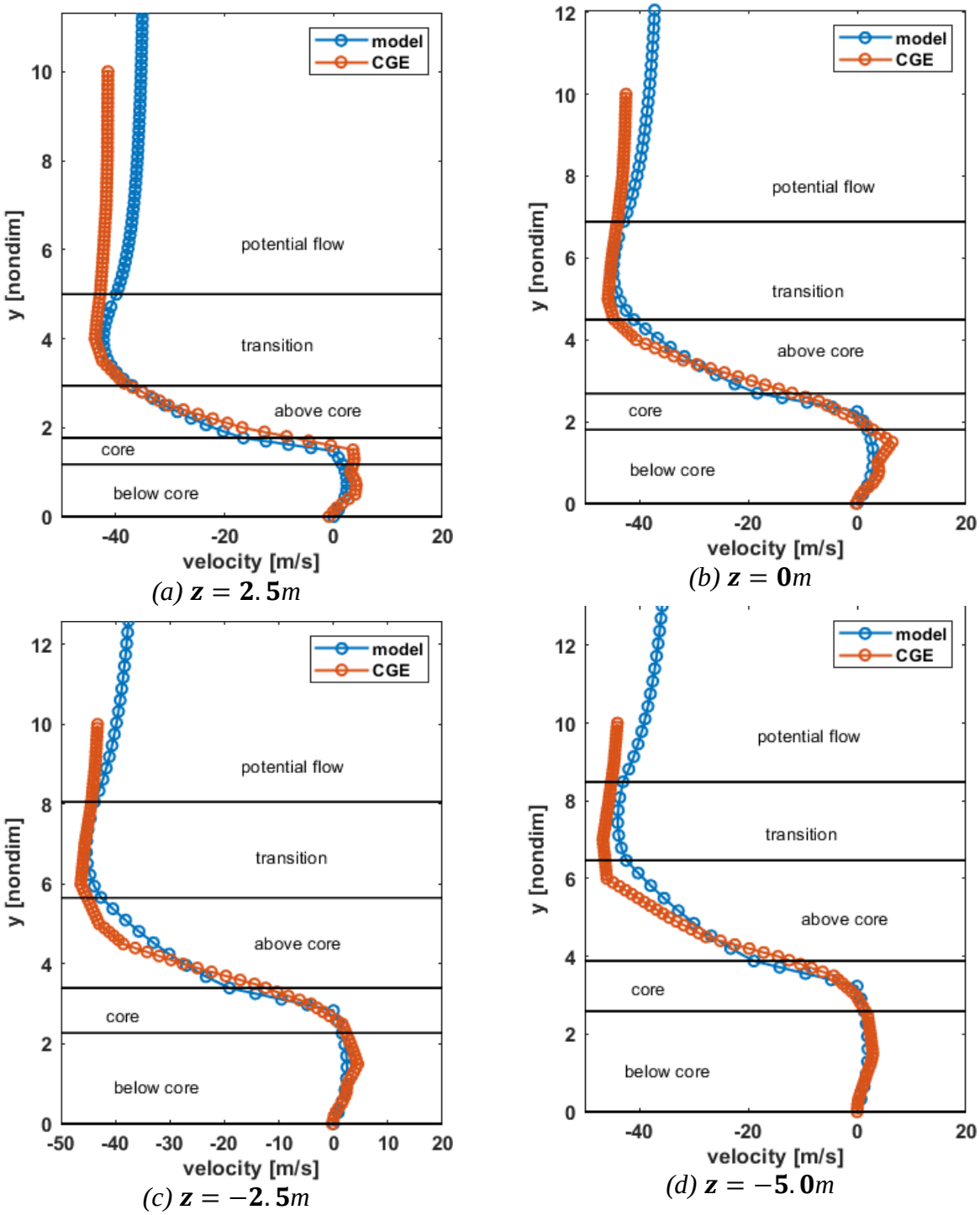

(a) $\boldsymbol{z = 2.5m}$ (b) $\boldsymbol{z = 0m}$

(c) $\boldsymbol{z = -2.5m}$ (d) $\boldsymbol{z = -5.0m}$

Figure 16: Velocity profile at various longitudinal span locations for a 40m/s headwind.

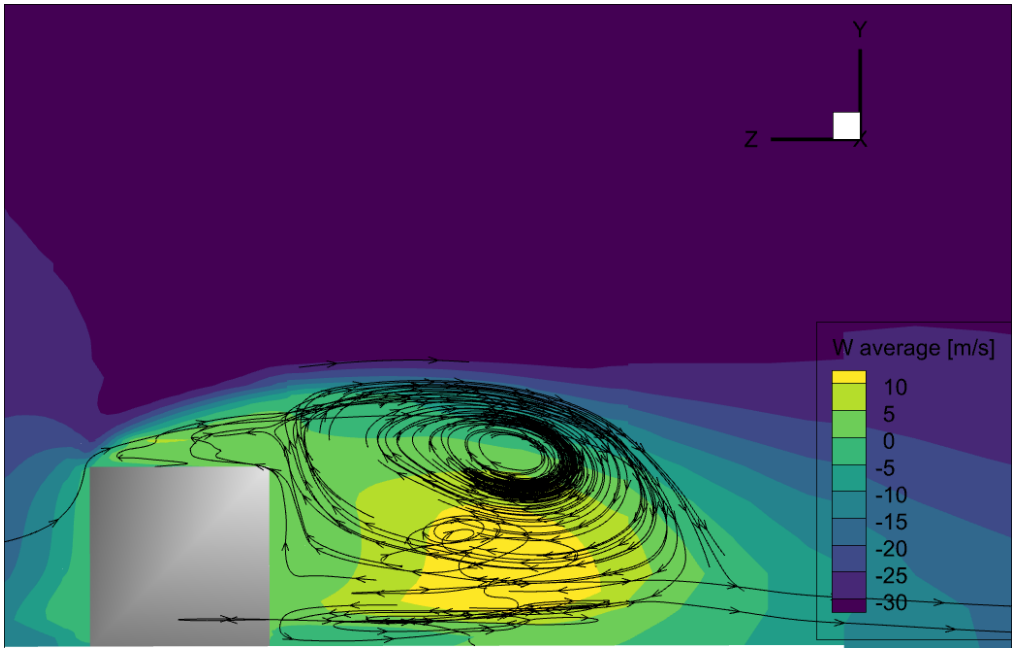

Figure 17: Contour of time-averaged longitudinal velocity profile along midplane with streamlines indicating presence of aft of the obstacle.

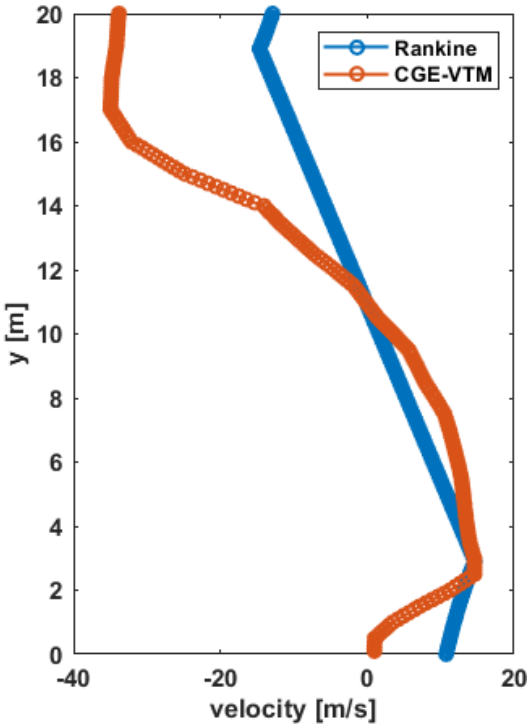

Figure 18: Rankine vortex-based velocity profile along vertical line through vortex center.

A modified version of the Banks and Meroney model [16, 17] introduced in the previous section was found to produce a better agreement. The equations in Table 1 were still applied but in this case, the vortex was shifted upwards such that a transition region existed below the vortex center as well, as depicted in Figure 19. With this shift, the vortex model can be thought of as

wheel being spun at two points: point M_{upper} at a velocity $U_{M_{upper}}$ and point M_{lower} at a velocity $U_{M_{lower}}$. Inputs to the model thus consisted of

1. the vortex radius (h),
2. the location of points M_{upper} and M_{lower} (assumed to be equidistant from the vortex center)
3. the velocity at point M_{upper} ($U_{M_{upper}}$) and
4. the velocity at point M_{lower} ($U_{M_{lower}}$).

To maintain the piece-wise continuity of the vortex model velocity profile predictions, the maximum velocity U_{max} (see Table 1) used in the core, below core, and lower transition regions was set equal to $U_{M_{lower}}$. In the upper transition and potential flow regions, U_{max} was set equal to $U_{M_{upper}}$. In the above core region, linear interpolation between $U_{M_{lower}}$ and $U_{M_{upper}}$ was used to determine U_{max}. Two additional modifications were made to the vortex model introduced in the previous section:

1. the location where the maximum velocity was obtained in the transition region (a_{max}) was changed from the midpoint location to the end point of the transition region; and
2. the size of the vortex core was increased from $0.2h$ to $0.4h$.

Velocity predictions in the region below the lower transition were obtained using linear interpolation between the velocity at point M_{lower} and 0 m/s at a point y_0, below which the velocity was assumed to be zero. Vortex parameters and resulting velocity profiles are shown in Table 4 and Figure 20, respectively, where the model shows good agreement with the velocity profile predicted by CGE/VorTran-M, with a maximum deviation of approximately 7 m/s noted at $y = 14$ m.

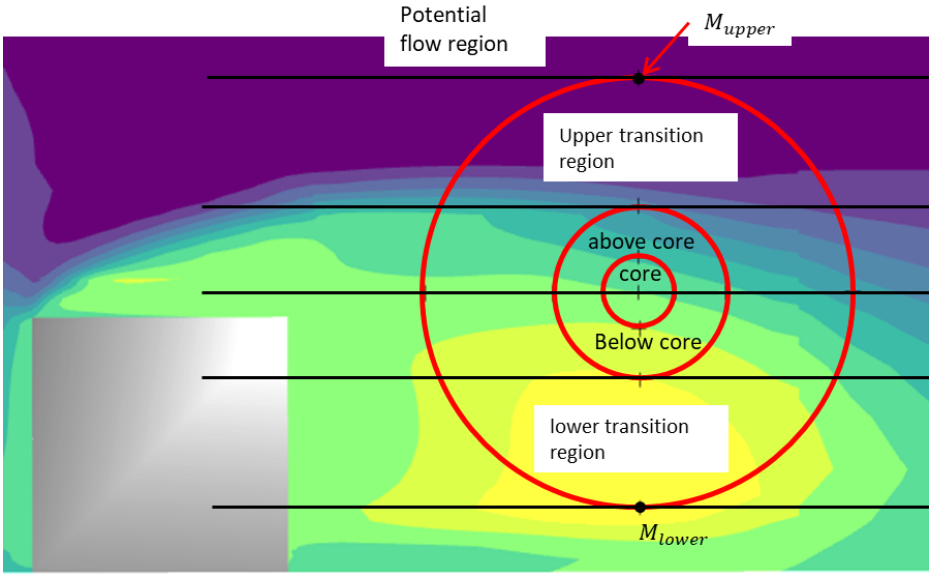

Figure 19: Illustration of modified Banks and Meroney vortex model shifted upwards.

Table 4: Modified vortex model parameter values; distances specified relative to global CGE coordinate system.

Parameter	Value
h (m)	3.4
R_M (m)	8.4
$U_{M_{lower}}$ (m/s)	-14.7[1]
$U_{M_{upper}}$ (m/s)	-34.2
y_0 (m)	0.5

[1] Value was negated to obtain correct profile.

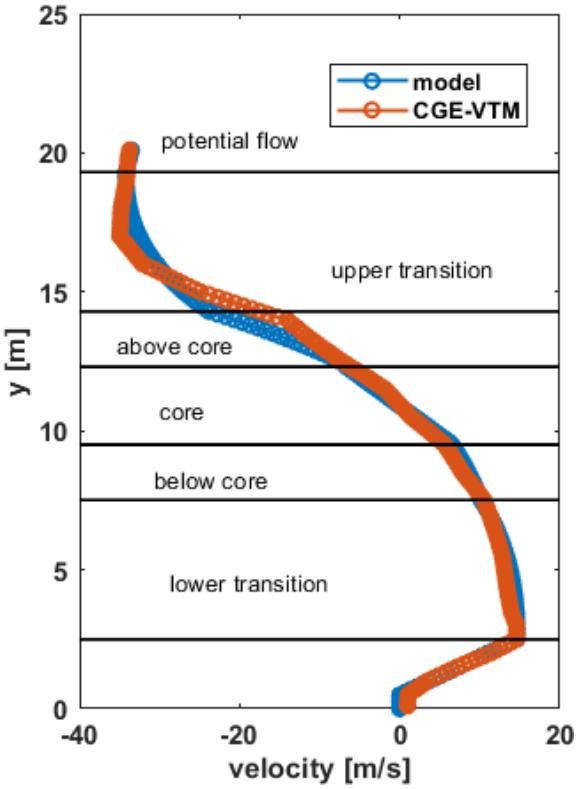

Figure 20: Longitudinal velocity profile along a vertical line through vortex center in the lee of the cube.

Next, velocity profiles along radial lines at $\theta = \{30°, 45°, 135°, 150°\}^T$ were considered, where θ is measured counterclockwise from an axis z', which has its origin at the vortex center and is parallel to the global CGE z axis shown in the contour plots above. We found that a circular vortex model, as depicted in Figure 19, failed to fully capture the velocity predictions from CGE/VorTran-M (see Figure 21). Reasonable agreement is noted for $\theta = 135°$ and $\theta = 150°$ in Figure 21, but large discrepancies are noted for the $\theta = 30°$ and $\theta = 45°$ cases. These discrepancies are attributed to the influence of the top surface separation considered in the previous section, and the corresponding vortex model parameters are summarized in Table 5. Note that longitudinal velocity values were used as rotational velocities $U_{M_{lower}}$ and $U_{M_{upper}}$. Using tangential velocities resulted in significant offsets in model predictions.

Table 5: Modified vortex model parameter inputs for the radial lines considered.

Parameter	$\theta = 30°$	$\theta = 45°$	$\theta = 135°$	$\theta = 150°$
h (m)	3.4	3.4	3.4	3.4
R_M (m)	8.4	8.4	8.4	8.4
$U_{M_{lower}}$ (m/s)	-2.5[1]	-8.0[1]	-8.9[1]	-7.0[1]
$U_{M_{upper}}$ (m/s)	-20.9	-34.7	-31.8	-28.2
y_0 (m)	0.5	0.5	0.5	0.5

[1] Values negated to obtain profile.

To better match CGE/VorTran-M velocity predictions, we then investigated the use of an ellipse-shaped vortex following the streamline pattern shown in Figure 17. The dimensions in Table 4 were used to define the semi-minor radii, and the semi-major radii were obtained by applying a scaling factor to the semi-minor radius values. A scaling factor value of 3.3 was used in this work based on manual tuning. The ellipse-based vortex was also assumed to have a built-in slant angle γ, measured counterclockwise relative to the z' axis. Using position coordinates of several points along the streamlines shown in Figure 17, the slant angle was determined to be approximately $16°$. The resulting vortex shape is illustrated Figure 22.

Velocities obtained using the ellipse-based vortex model are shown in Figure 23. Results show good agreement with predictions from CGE/VorTran-M, with the largest discrepancies again noted for the $\theta = 30°$ and $\theta = 45°$ cases. These discrepancies, however, are significantly less pronounced than those noted in Figure 21.

It is important to clarify here that this "elliptical vortex" is a mathematical modeling construct that was found to better represent the CFD source data in the recirculation region. Physically, such a construct does not exist but can be viewed as an approximation of a vortical structure in which the vorticity is distributed over a spatial dimension (e.g., a vortex line or sheet). In this physical case, the actual velocity field associated with this vortical structure may not be precisely elliptical in shape, depending on the distribution of vorticity. This distinction is not deemed critical to the formulation of the canonical airwake models at the moment, but will be re-examined as necessary.

Note further that the velocities $U_{M_{lower}}$ and $U_{M_{upper}}$ were initially probed manually from Tecplot. To facilitate the vortex model fitting process, the value of $U_{M_{lower}}$ at a given span location aft of the cube was set to the maximum longitudinal velocity along the vertical line at that location. Similarly, $U_{M_{upper}}$ was set to the minimum longitudinal velocity. These definitions are based on the CGE problem setup, where freestream is in the negative z direction. A Tecplot macro script was used to query the velocity profiles at various span location aft of the cube, which were then post-processed to obtain quadratic functions $U_{M_{lower}}(z)$ and $U_{M_{upper}}(z)$. These functions were used to generate the profiles in Figure 23.

Although this ellipse-based vortex fit showed good agreement for radial lines at nonzero θ angles, it failed to capture the velocities along z span locations that did not traverse all three vortex regions shown in Figure 22, producing good predictions primarily in the $-23 \leq z \leq -15$ m region. Further tuning of the model was performed, and better predictions were obtained using a semi-minor radius to semi-major radius of 10 and a slant angle of approximately 8°. The resulting vortex shape is illustrated Figure 24. Note that the vortex core region only extends to

$z \approx -32$ m downstream of the obstacle. Velocity predictions were obtained using a coordinate system that has its origin at the center of the ellipse, as illustrated in Figure 25. At any given span location, it was assumed that the radial coordinate from the center of the ellipse to any point below the intersection point between the ξ axis and the vertical line at the span location was negative. Similarly, any radial coordinate above the intersection point was positive. This sign convention was adopted for consistency with the Banks and Meroney model equations shown in Table 1.

Velocities obtained using the updated ellipse-based vortex model are shown in Figure 26 and Figure 27. Results show good agreement with prediction from CGE/VorTran-M up to $z = -26$ m. Apart from velocity predictions at $z = -18$ m, a kink in the predictions is noted in the core region at all span locations in Figure 26. This is due to the sudden switch in radial coordinate sign from negative to positive at those locations. The $z = -18$ m location is close to the vortex center ($z = -18.8$ m) and thus the magnitude of the radial coordinate at the intersection of the ξ axis and the vertical line at $z = -18$ m is relatively small (see Figure 25). From Figure 26 and Figure 27, predictions from the model deteriorate downstream from $z = -26$ m onwards. Sharp changes in velocities are also noted beyond $z = -30$ m, where the vortex core region does not exist (see Figure 24).

To better match CGE/VorTran-M predictions beyond $z = -26$ m, a secondary vortex model was adopted in this downstream region. This model follows a similar structure to that presented for the top surface separation above and assumes that an infinite number of overlapping vortices of differing sizes exist in the downstream region. Linear functions for the vortex center location $y_0(z)$, vortex radius $h(z)$, vortex core fraction $c(z)$, and location of $M_{upper}(z)$ were derived by manually tuning vortex model parameters at various z locations aft of $z = -26$ m:

$$y_0(\bar{z}) = -0.1514\bar{z} + 11.481, \tag{5}$$

$$h(\bar{z}) = 0.2045\bar{z} + 3.7321, \tag{6}$$

$$c(\bar{z}) = 0.0124\bar{z} + 0.4, \tag{7}$$

$$M_{upper}(\bar{z}) = 0.0661\bar{z} + 8.604, \tag{8}$$

where $\bar{z} = z_1 - z$, with $z_1 = -26$ m. From Figure 27, the inviscid nature of the simulation is apparent from the nonzero velocities near the ground at span location downstream of $z = -26$ m. In practice, velocity near the ground would be close to zero. To better match the *inviscid* predictions, a linear function for the velocity near the ground was derived:

$$V_{y_0}(z) = -0.7252\bar{z} - 1.3413. \tag{9}$$

Velocity predictions in the region below the lower transition (see Figure 19) at a given span location were then obtained using linear interpolation between the velocity $U_{M_{lower}}(z)$ at point M_{lower} and $V_{y_0}(z)$ from Eq. (9) at point y_0, below which the velocity was assumed to be $V_{y_0}(z)$.

The combined use of the ellipse-based vortex model up to $z = -26$ m and the infinite vortex model beyond that location allowed for the velocity profile aft of the obstacle to be adequately captured as shown in Figure 28 and Figure 29. Note that the velocities in the core region in Figure 28 were obtained using an explicit linear interpolation between the velocity in the above core and below core regions to avoid the kinks seen in Figure 26.

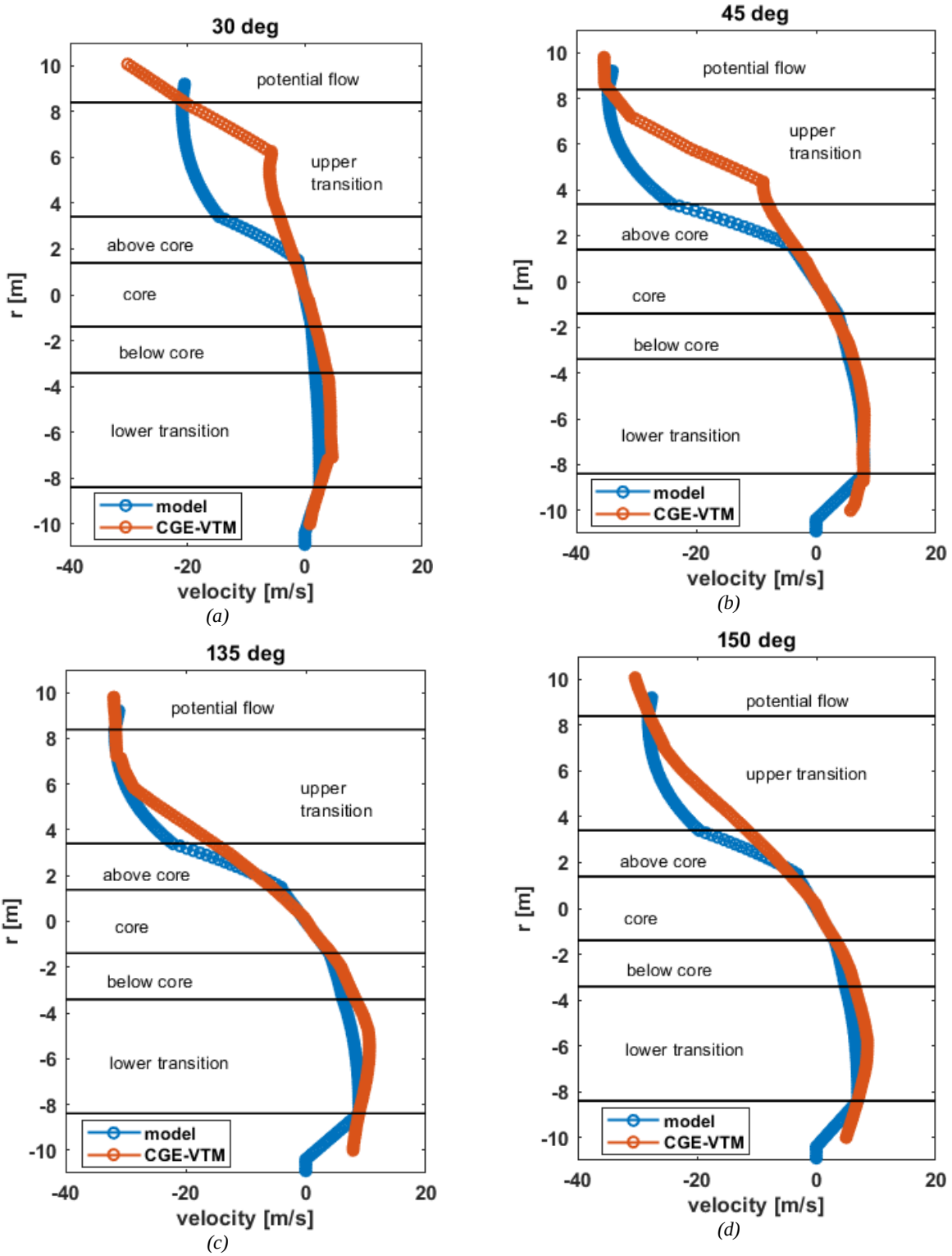

Figure 21: Velocity profiles along radial lines at nonzero angular displacements in the lee of the obstacle; vortex assumed to be circular.

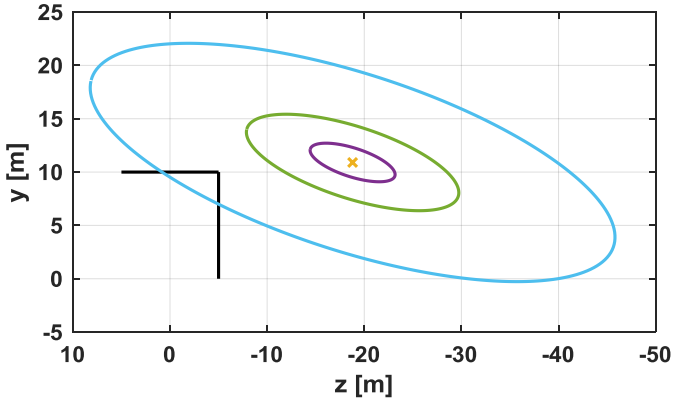

Figure 22: Illustration of the ellipse-based vortex; black line outlines the obstacle; orange cross indicates vortex center; purple line delimits vortex core; green line delimits vortex size; and blue line indicates the end of the transition region.

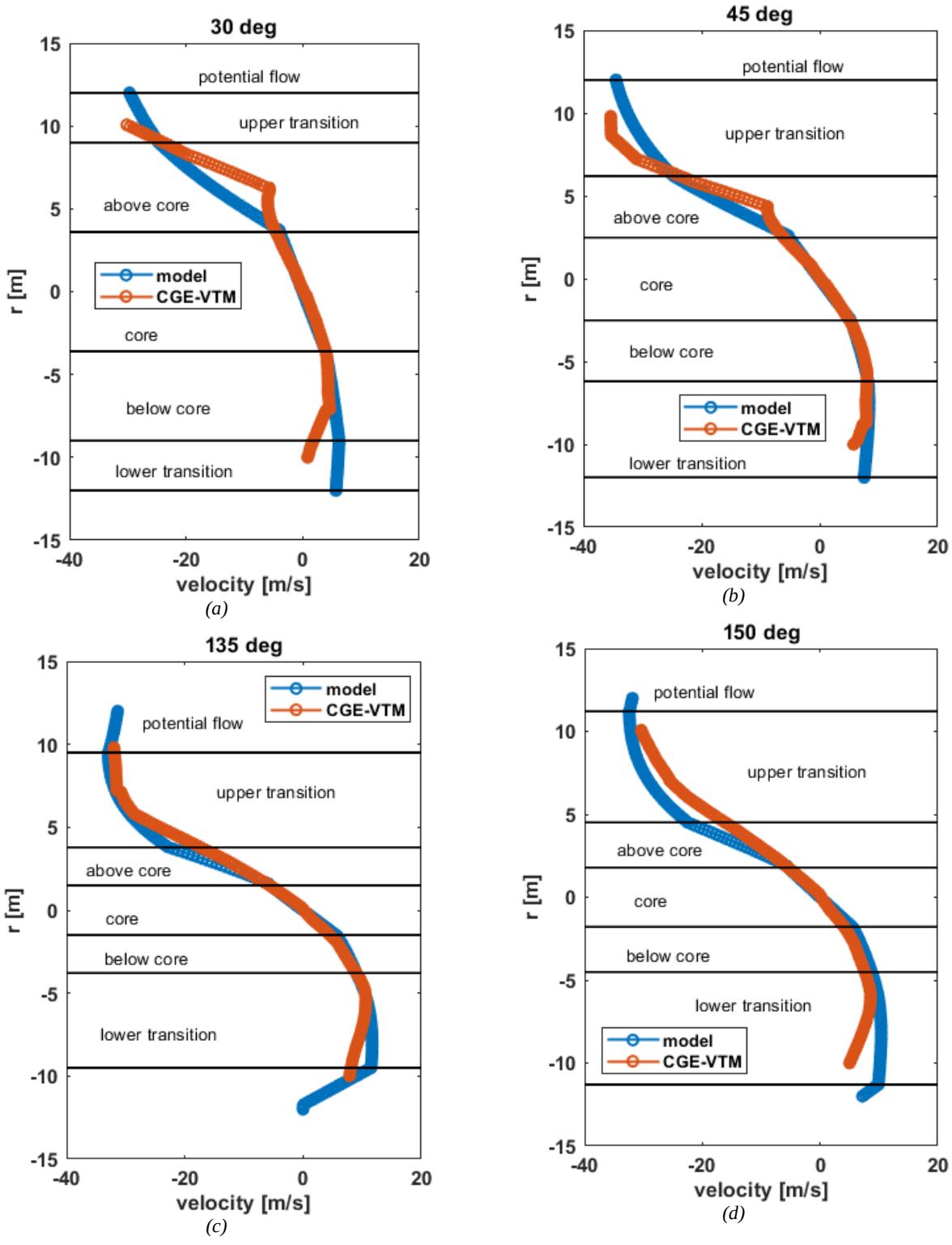

Figure 23: Velocity profiles along radial lines at nonzero angular displacements in the lee of the obstacle; vortex assumed to be a slanted ellipse.

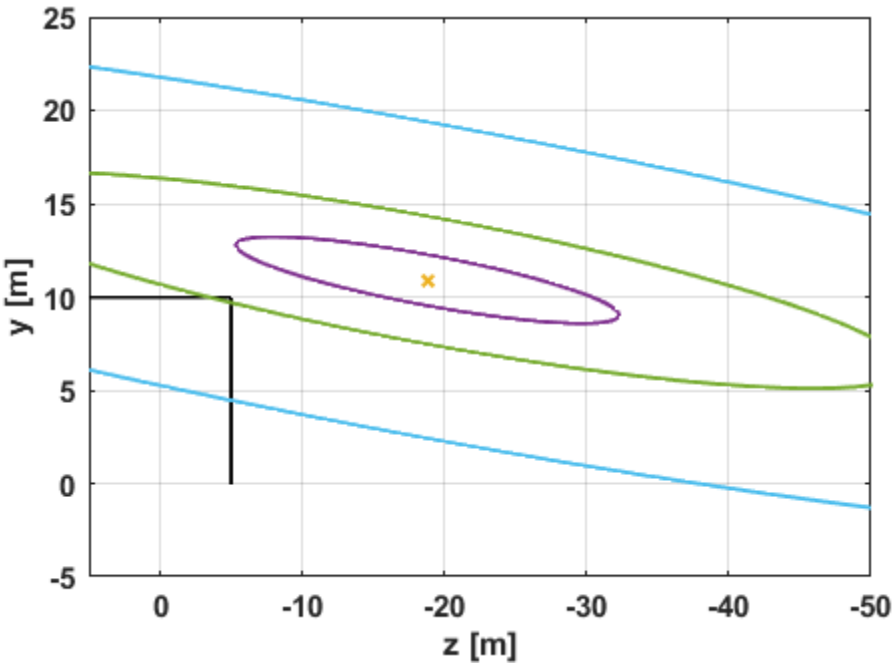

Figure 24: Illustration of modified ellipse-based vortex; black line outlines the obstacle; orange cross indicates vortex center; purple line delimits vortex core; green line delimits vortex size; and blue line indicates the end of the transition region.

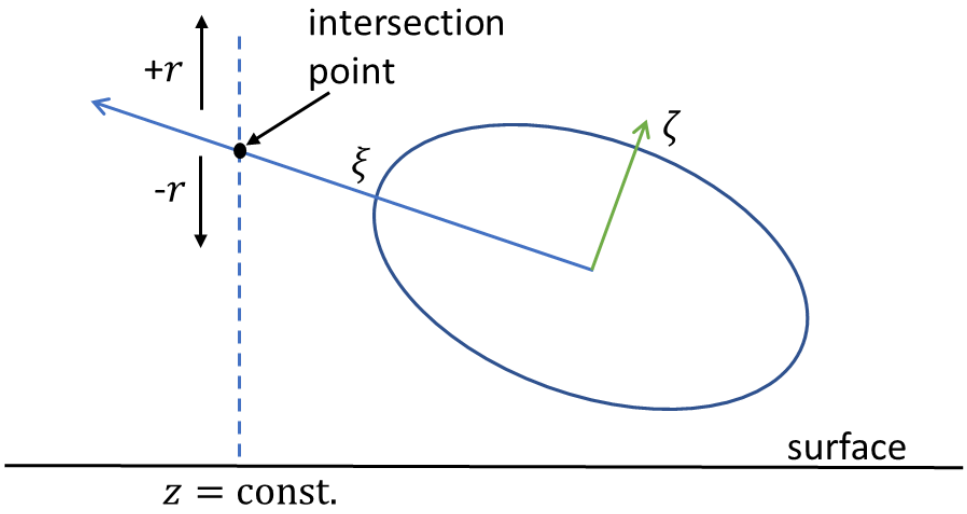

Figure 25: Illustration of slanted ellipse coordinate system and sign convention employed for radial coordinates from the center of the ellipse.

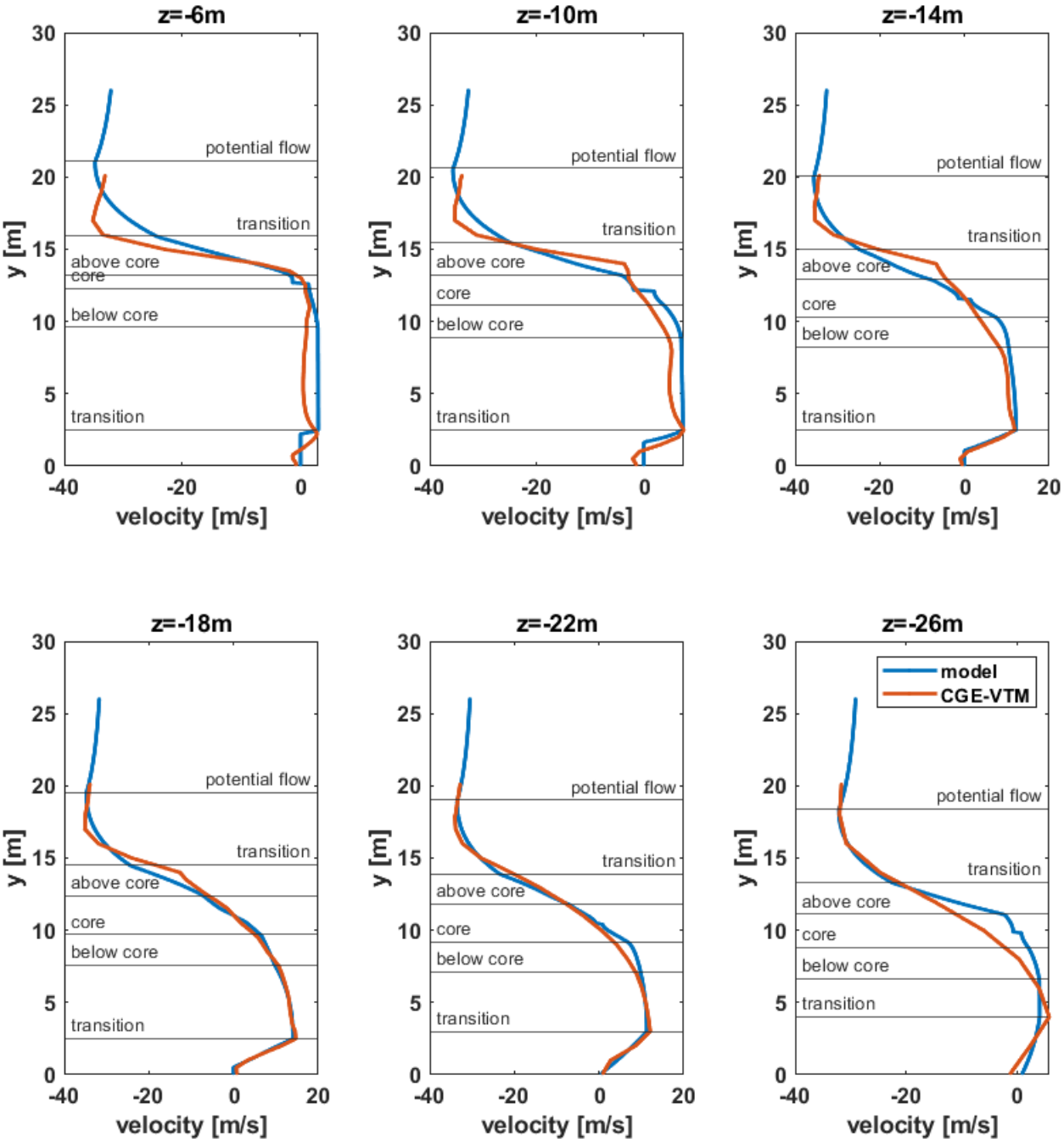

Figure 26: Longitudinal velocity profile at various span locations in the $-6\ m \geq z \geq -26\ m$ range aft of the obstacle along the $x = 0\ m$ plane; only the slanted ellipse-based vortex model used; CGE/VorTran-M data queried in 0.1 m height increments at every span location.

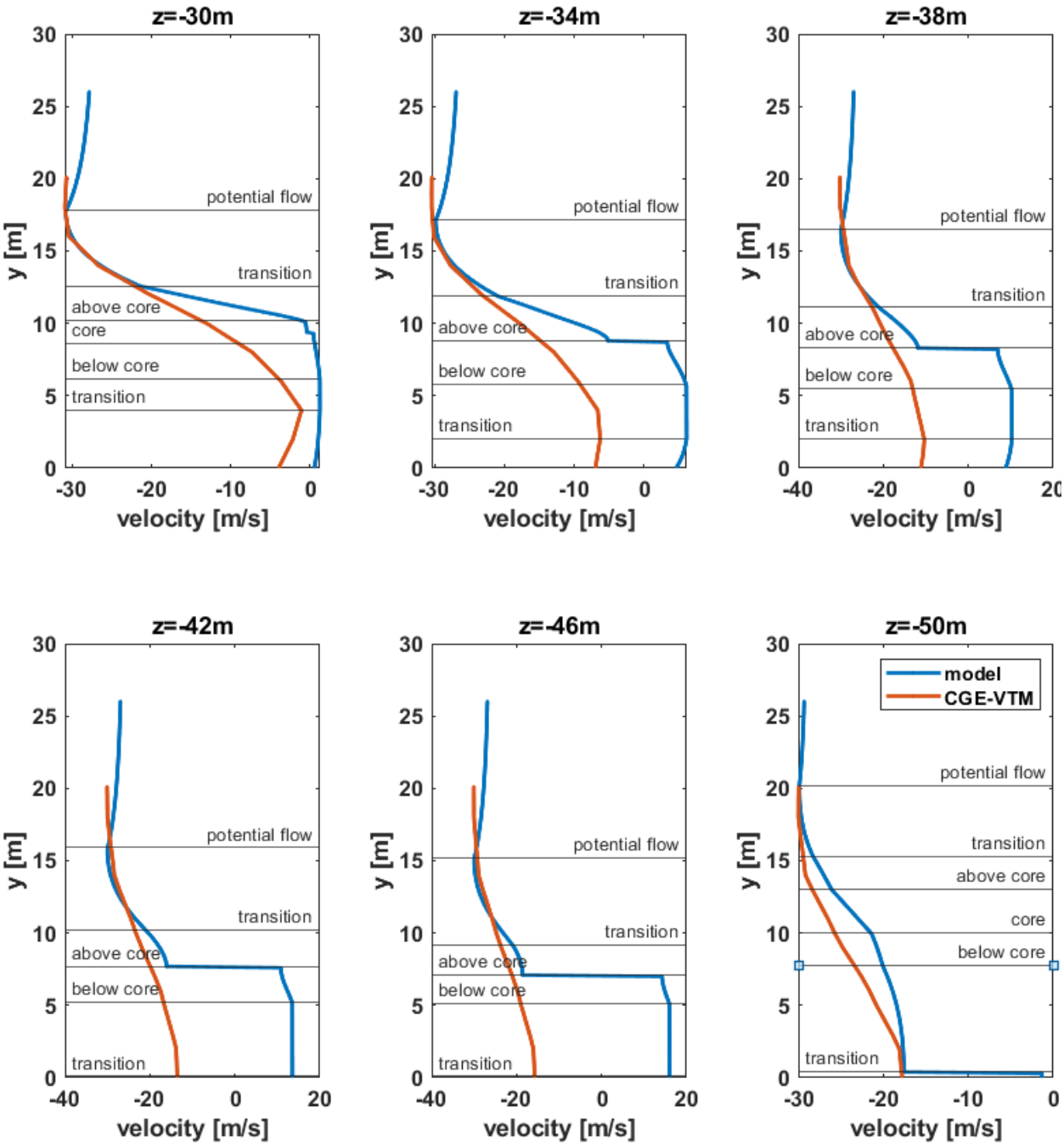

Figure 27: Longitudinal velocity profile at various span locations in the $-30\ m \geq z \geq -50\ m$ range aft of the obstacle along the $x = 0\ m$; only the slanted ellipse-based vortex model used; CGE/VorTran-M data queried in 0.1 m height increments at every span location.

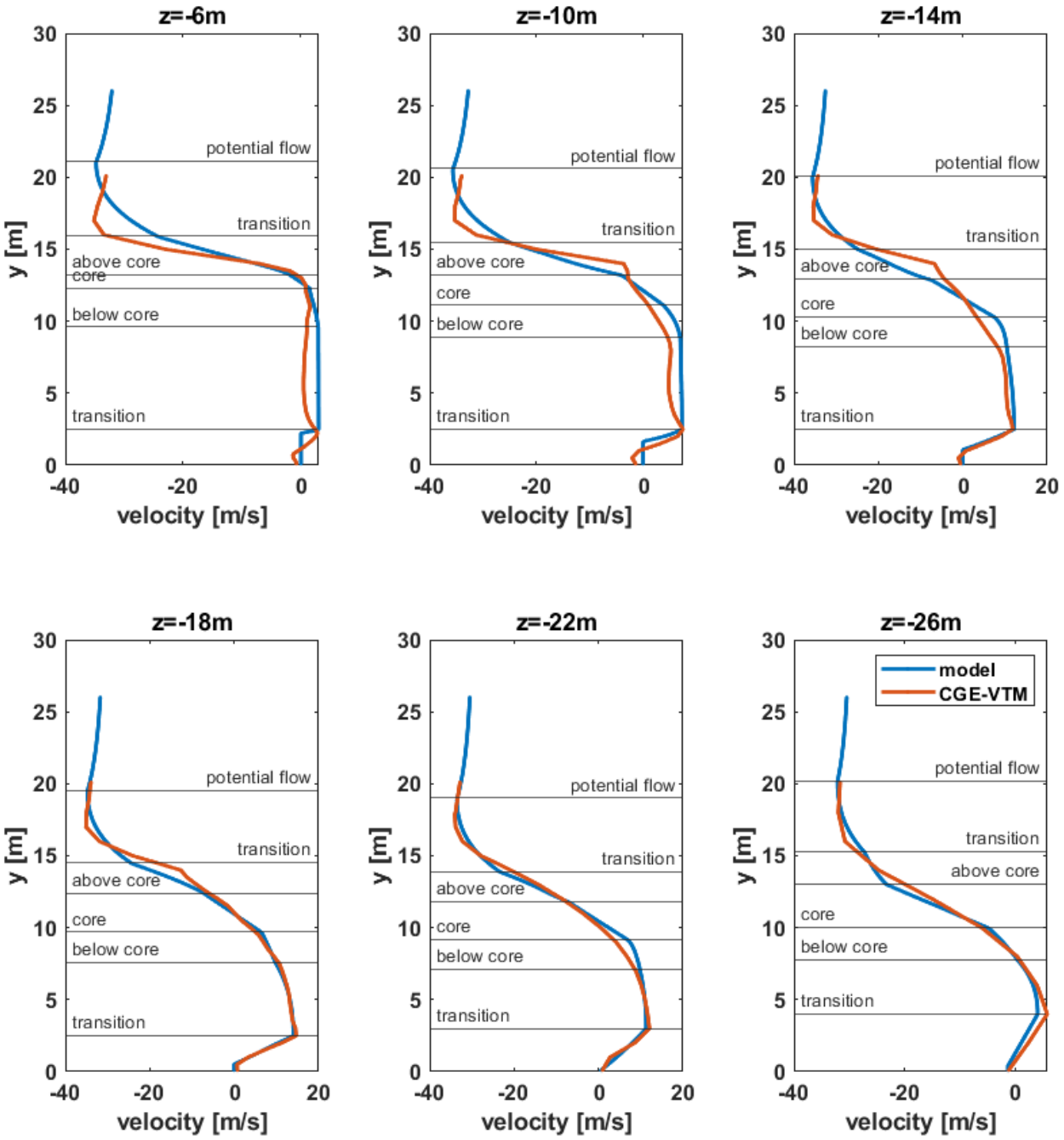

Figure 28: Longitudinal velocity profile at various span locations aft of the obstacle along the $x = 0$ m plane using the slanted ellipse-based vortex model for $-6\ m \geq z > -26\ m$ and the infinite vortex model for $z = -26\ m$; CGE/VorTran-M data queried in 0.1 m height increments at every span location.

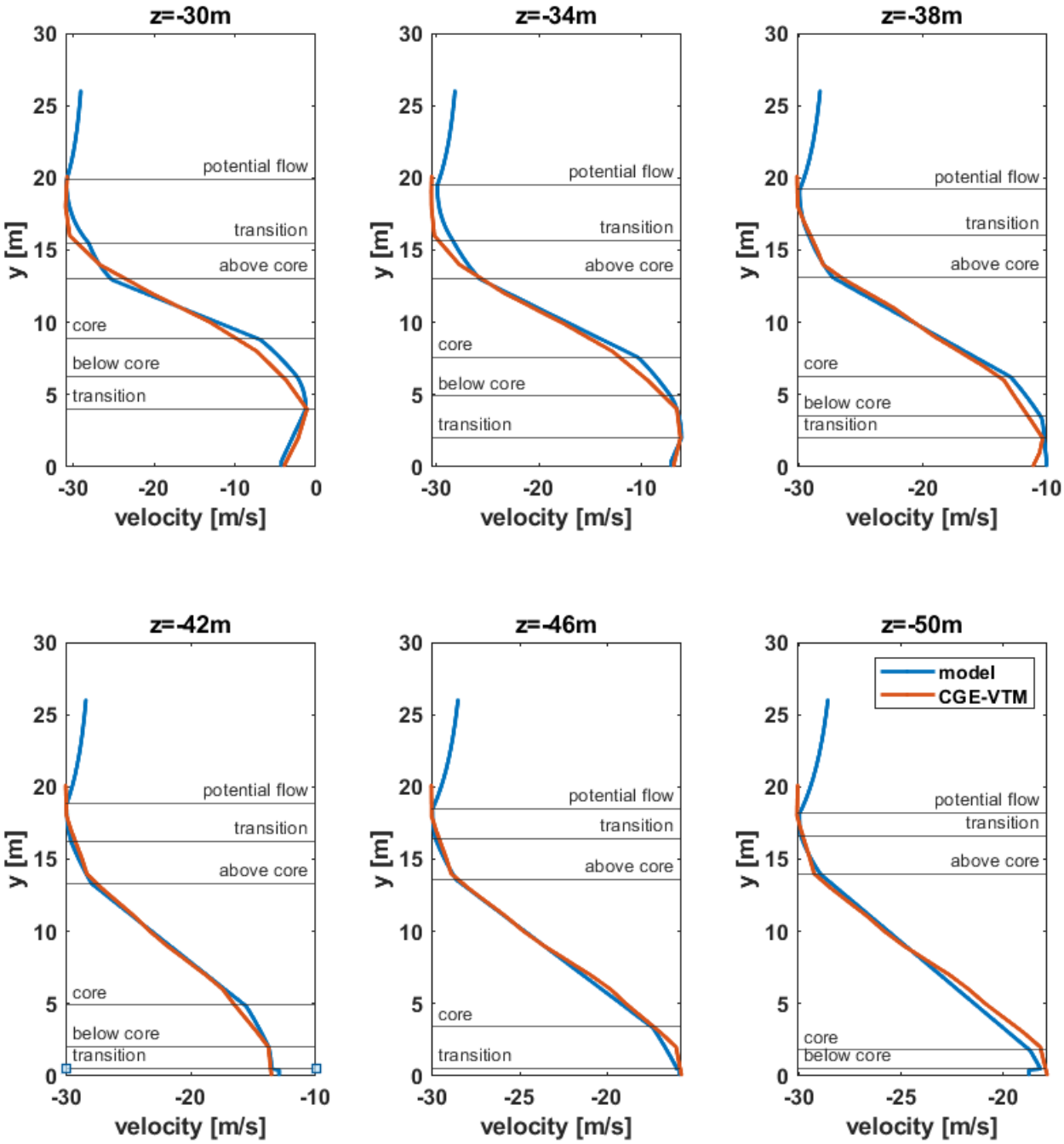

Figure 29: Longitudinal velocity profile at various span locations in the $-30\ m \geq z \geq -50\ m$ range aft of the obstacle along the $x = 0\ m$ plane using the infinite vortex model; CGE/VorTran-M data queried in 0.1 m height increments at every span location.

Side surface flow separation modeling

In addition to the top edge, flow also detaches at the side edges of the wind-facing surface and reattaches aft of the obstacle as depicted in Figure 2. A recirculation zone is created on the side surfaces due to interaction of the incoming freestream with this separation (see Figure 6(b) and Figure 30). Given the similarity of the side surface separation to the top surface separation considered previously, the infinite vortex model used to capture the velocity distribution across

the top surface was also employed here. Results are shown in Figure 31 across the $y = 5$ m plane for separation over the left surface ($x = 5$ m in Figure 30). Except for the region within a height of 1m from the side surface at z = 5 m, reasonable agreement with CFD predictions is obtained without any modifications to the model. The discrepancy within the 1m region from the surface was also noted for the top surface and is deemed acceptable given that in practice, it is unlikely that the aircraft will be flying that close to the building during approach or take-off.

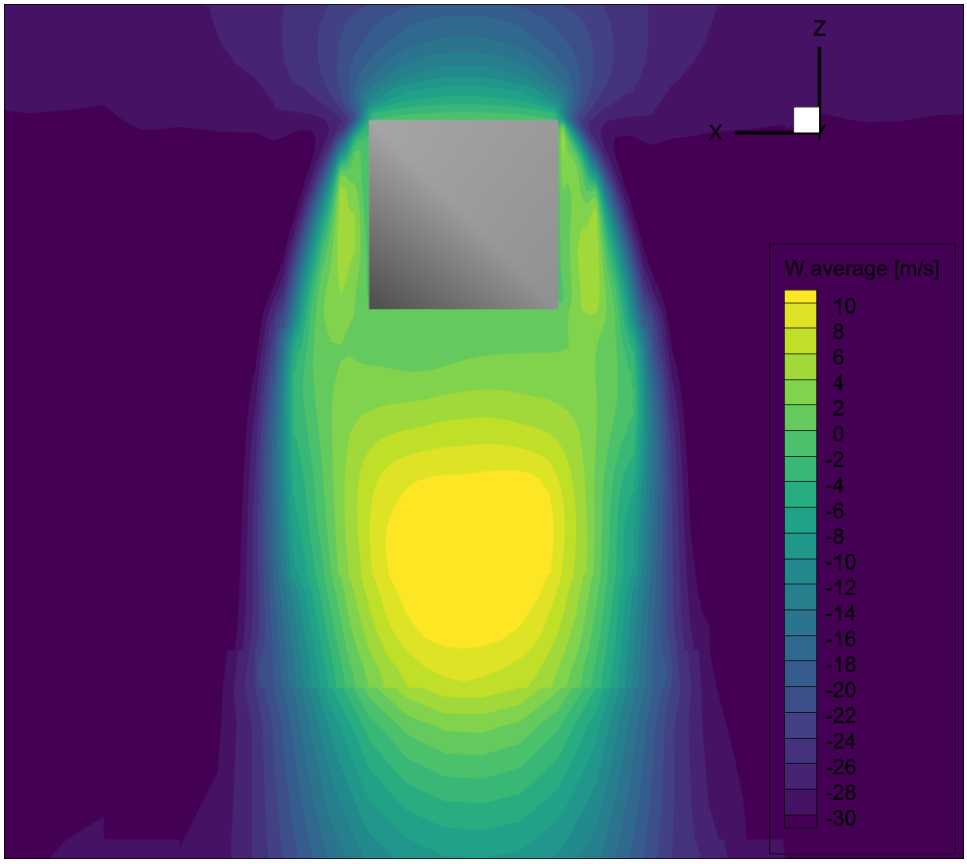

Figure 30: Contour of time-averaged longitudinal velocity for a 30m/s headwind simulation over a 10m cube using CGE/VTM along a midplane at $y = 5$ m (top view).

Aft of the cube, the von Karman streak shown in Figure 6(e) is only observed during *time-accurate* solutions. Contours of *time-averaged* longitudinal velocity instead display a symmetrical distribution aft of the obstacle, as evident in Figure 30. It was surmised that the piece-wise ellipse-based and infinite vortex model used for the backstep separation would be applicable here as well, with the primary difference being the starting height from where the velocity predictions would be made. In the previous section, velocity predictions were made from $\hat{y} = 0$ m given that this coordinate represents the ground surface. The $\hat{y}$ axis is introduced to represent vertical axis used by the model. For the backstep separation considered in the previous section, the vertical axis used by the model corresponded with the CGE/VorTran-M y axis shown in Figure 30, and thus $\hat{y} = y$. In the current side surface separation case, $\hat{y} = x$. Unlike the backstep separation case, no ground is present in the current case, but a symmetry condition exists along the $x = 0$ m plane. From manual tuning, start heights of 0.4H and 0.25H for the ellipse-based and infinite vortex models, respectively, were found to produce reasonable agreement with prediction from the CGE/VorTran-M simulation as shown in Figure 32 and

Figure 33, where velocity distributions at various span locations for $x > 0$ m (left) are shown. Large discrepancies of approximately 15 m/s are noted at $z = -6$ m in the above core and transition regions, but those are deemed acceptable since it is unlikely that the aircraft would be flying at that location. Offsets between model CGE/ VorTran-M predictions remain ≤3 m/s at the remaining span locations. Similar results are obtained for the $x < 0$ m (right) region (not shown for brevity). With regards to parametrization, the results presented for the side flow separation are promising in that we were able to obtain adequate predictions for this flow feature by simple modifications to the inputs of the analytical vortex models for the backstep flow separation.

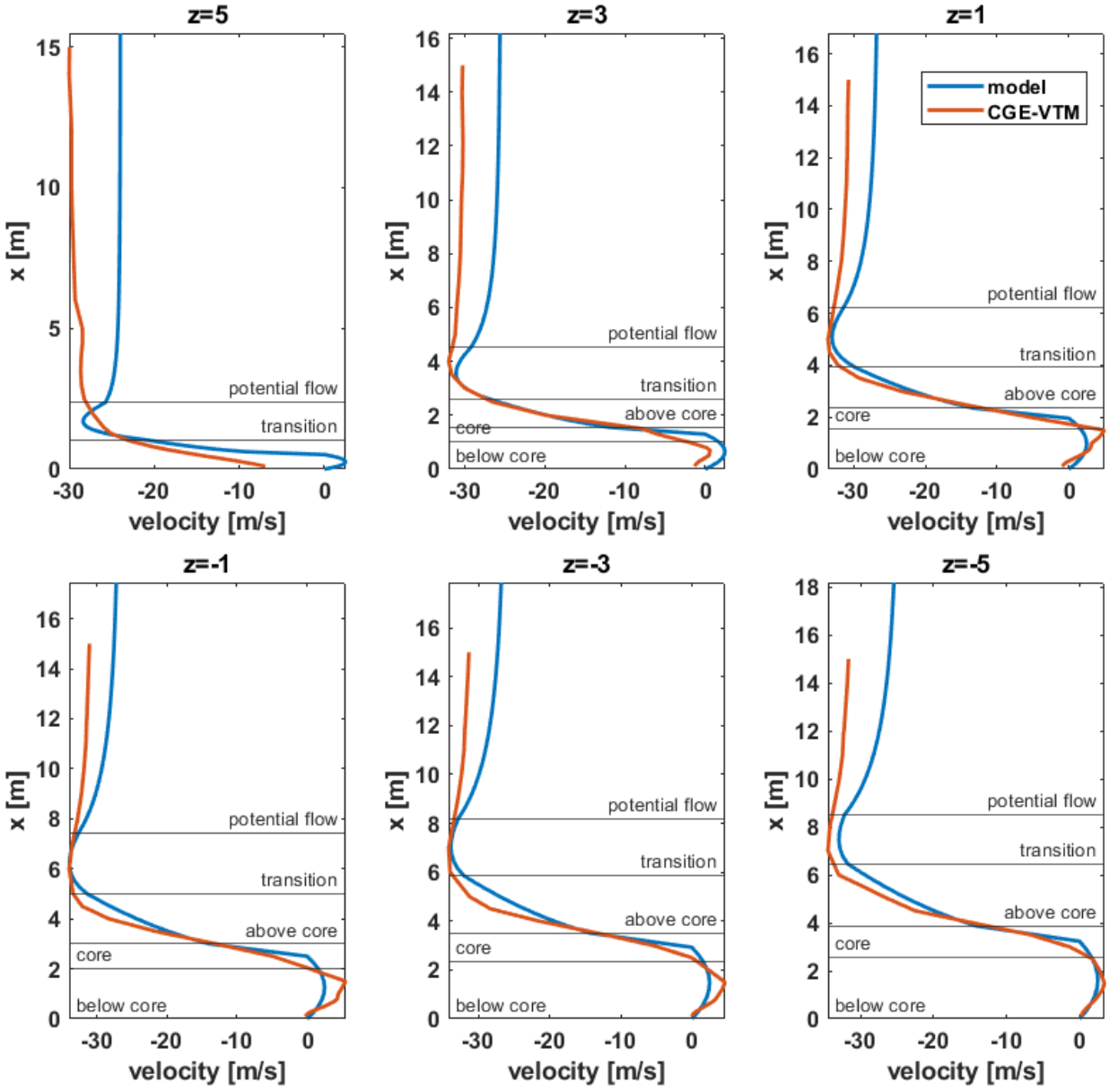

Figure 31: Longitudinal velocity profile over left side surface of cube ($\boldsymbol{x} = \mathbf{5}$ m); $\boldsymbol{x}$ distance plotted relative to surface; CGE data queried in 0.1 m increments at every span location.

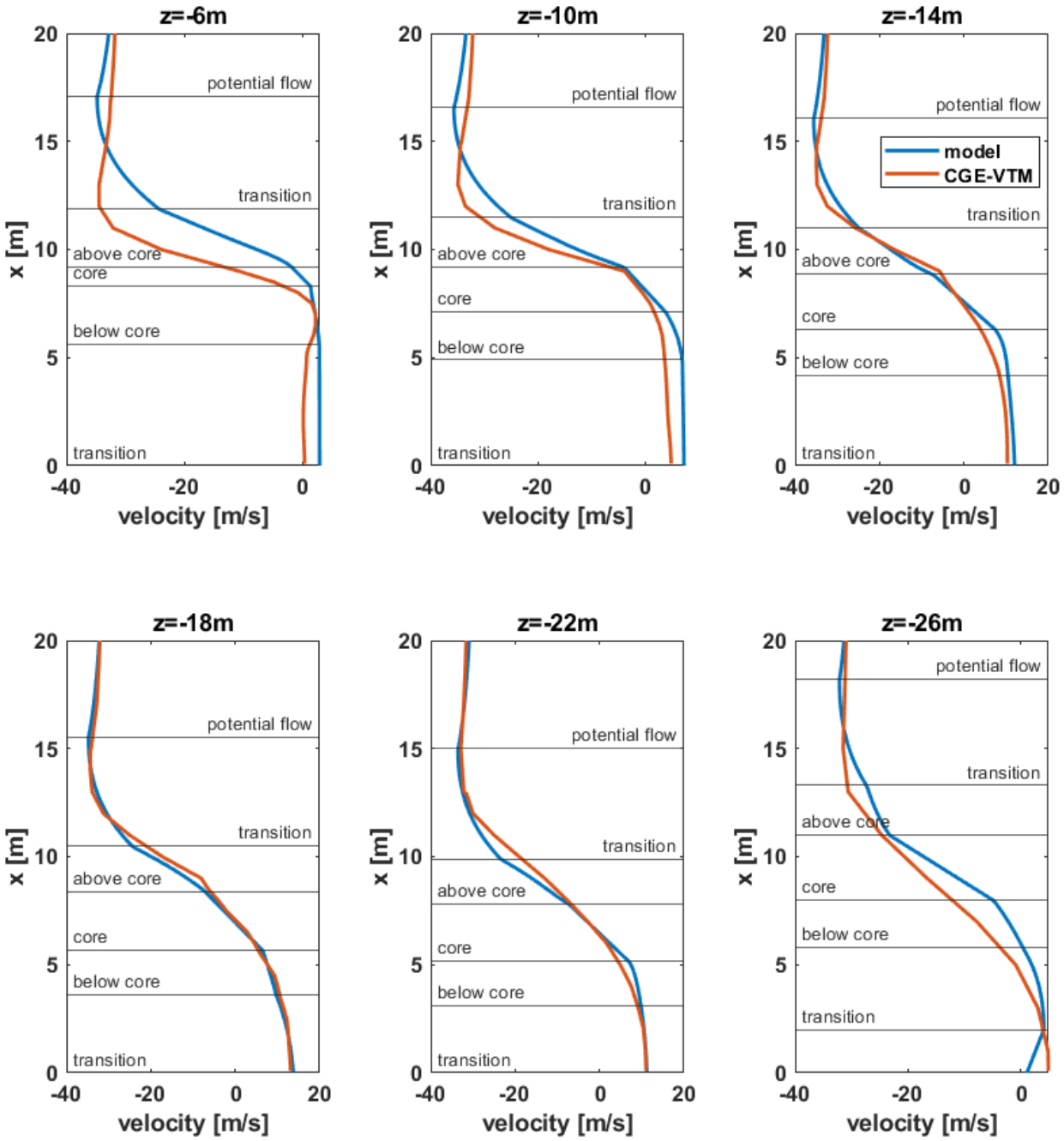

Figure 32: Longitudinal velocity profile at various span locations aft of the obstacle for $x > 0$ m along the $y = 5$ m plane using the slanted ellipse-based vortex model for $-6\ m \geq z > -26\ m$ and the infinite vortex model for $z = -26$ m; CGE/VorTran-M data queried in 0.1 m increments at every span location.

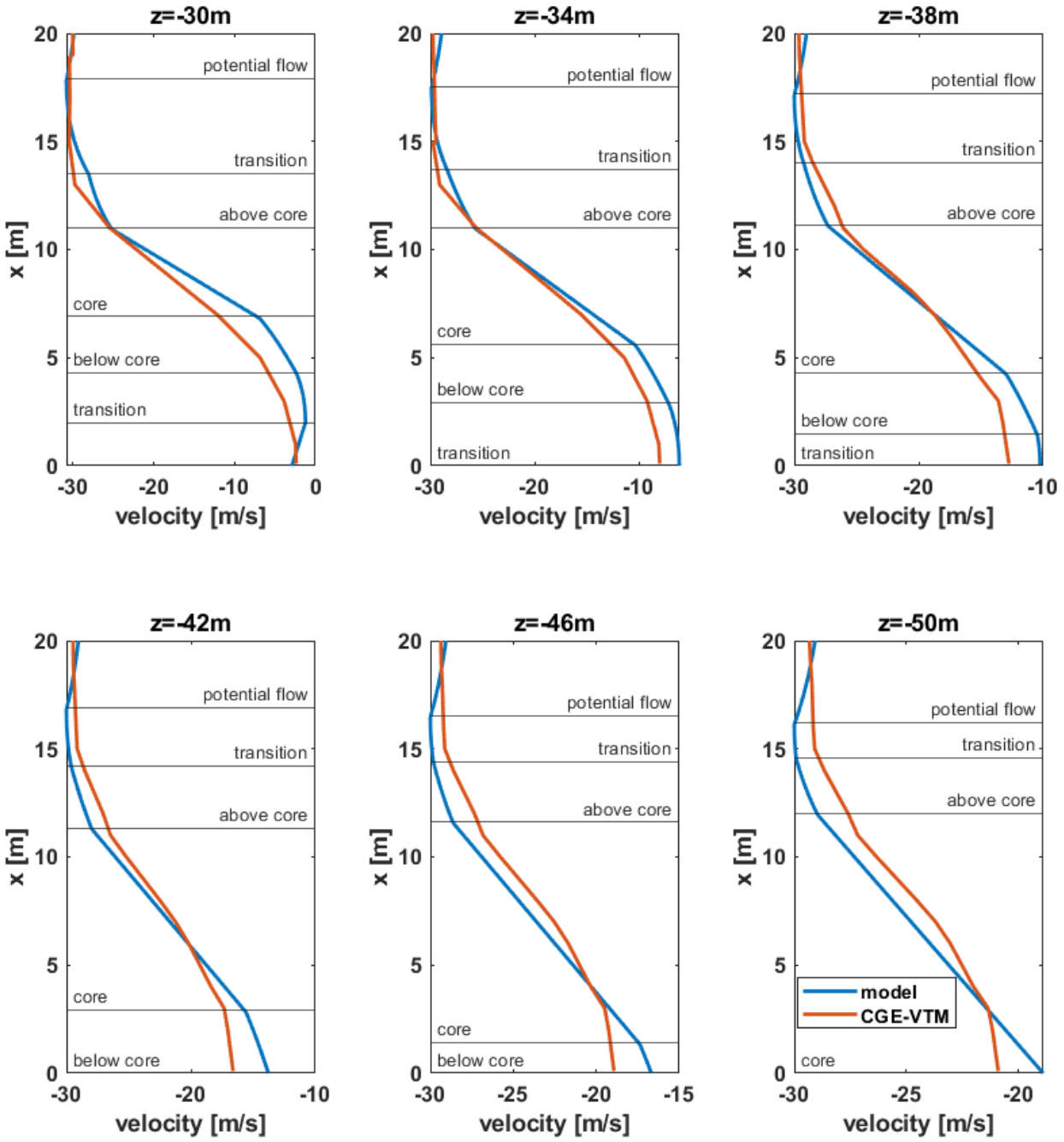

Figure 33: Longitudinal velocity profile at various span locations in the $-30\ m \geq z \geq -50\ m$ range aft of the obstacle for $x > 0\ m$ in the $y = 5\ m$ plane using the infinite vortex model; CGE/VorTran-M data queried in 0.1 m increments at every span location.

Corner flow separation modeling

For headwind flow conditions, edge vortices develop due to pressure gradients between side and top surfaces of the obstacle as illustrated in Figure 6(f). These edge vortices closely resemble roof corner vortices that the model was derived for, and thus, the original model equations shown in Table 1 were found to be applicable. Model inputs consist of the (1) the vortex radius (h), (2) the location of point M (R_M), and (3) the velocity at point M (U_M). Model

parameter values and the corresponding velocity profile are shown in Table 6 and Figure 34, respectively, for the dashed 45° line shown in Figure 35. Good agreement is noted between the model predictions and those from CGE/VorTran-M.

Table 6: Vortex model parameter values.

Parameter	Value
h (m)	1.5
R_M (m)	6.0
U_M (m/s)	-32.8

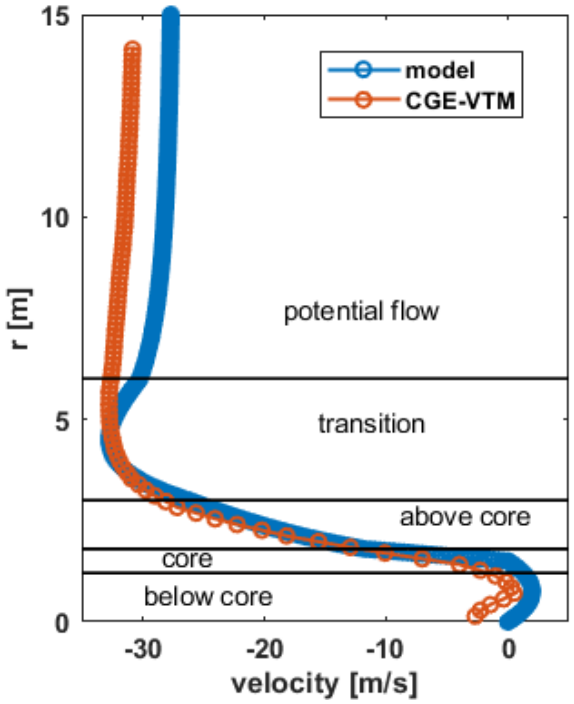

Figure 34: Longitudinal velocity profile along a 45° radial line from the corner of the cube.

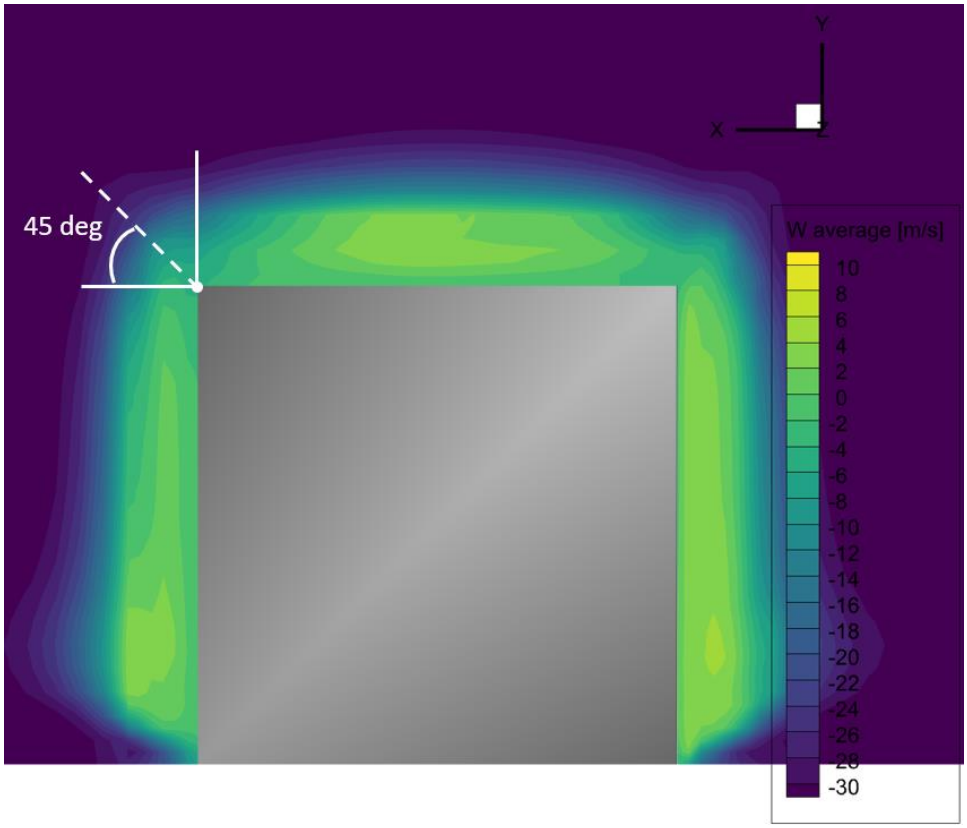

Figure 35: Contour of time-averaged longitudinal velocity for a 30 m/s headwind simulation over a 10 m cube along $z = 0$ m plane; dashed line represents line along with corner vortex model fitting was initially performed.

In a similar manner to the top surface separation, the 1D prediction along the 45° line was extended to cover the entire 2D region over the surface ($-5 \leq z \leq 5$ m). Here however, a function for the radial location of the vortex center $r_0(z)$ was also derived in addition to functions for the vortex radius $h(z)$, location of vortex rotation point $R_M(z)$, and velocity $U_M(z)$, which represent standard inputs of the vortex models:

$$h(\bar{z}) = 0.07\bar{z} + 1, \tag{10}$$

$$R_M(z) = 0.24\bar{z} + 3.2, \tag{11}$$

$$V_M(\bar{z}) = -0.0014\bar{z}^2 + 0.251\bar{z} + 1.004, \tag{12}$$

$$r_0(\bar{z}) = \min[-0.024\bar{z}^2 + 0.456z - 0.46, h(\bar{z})] \tag{13}$$

where $\bar{z} = z_{LE} - z$, and where the leading-edge span location $z_{LE} = 5$ m. From Eq. (13), the vortex center position can result in the vortex overlapping with the obstacle but is constrained to always being in contact with the edge. That is, there cannot be a gap between the vortex and the edge. This definition allowed for behavior at the $z = 5$ m (leading edge) location to be adequately captured, as evident in Figure 36. At this location, the vortex center is located "inside" the obstacle along the 45° line. As flow progresses further downstream over the obstacle, both the location of the vortex center and vortex size increase radially in Figure 36, in a manner that parallels the expected physical behavior of the corner edge vortices. The model thus

allows for physical insights into the flow phenomenon. Note that leading edge flow profiles for top and side surfaces separations can also potentially be captured by introducing $r_0(z)$ as an additional input to the fitting models.

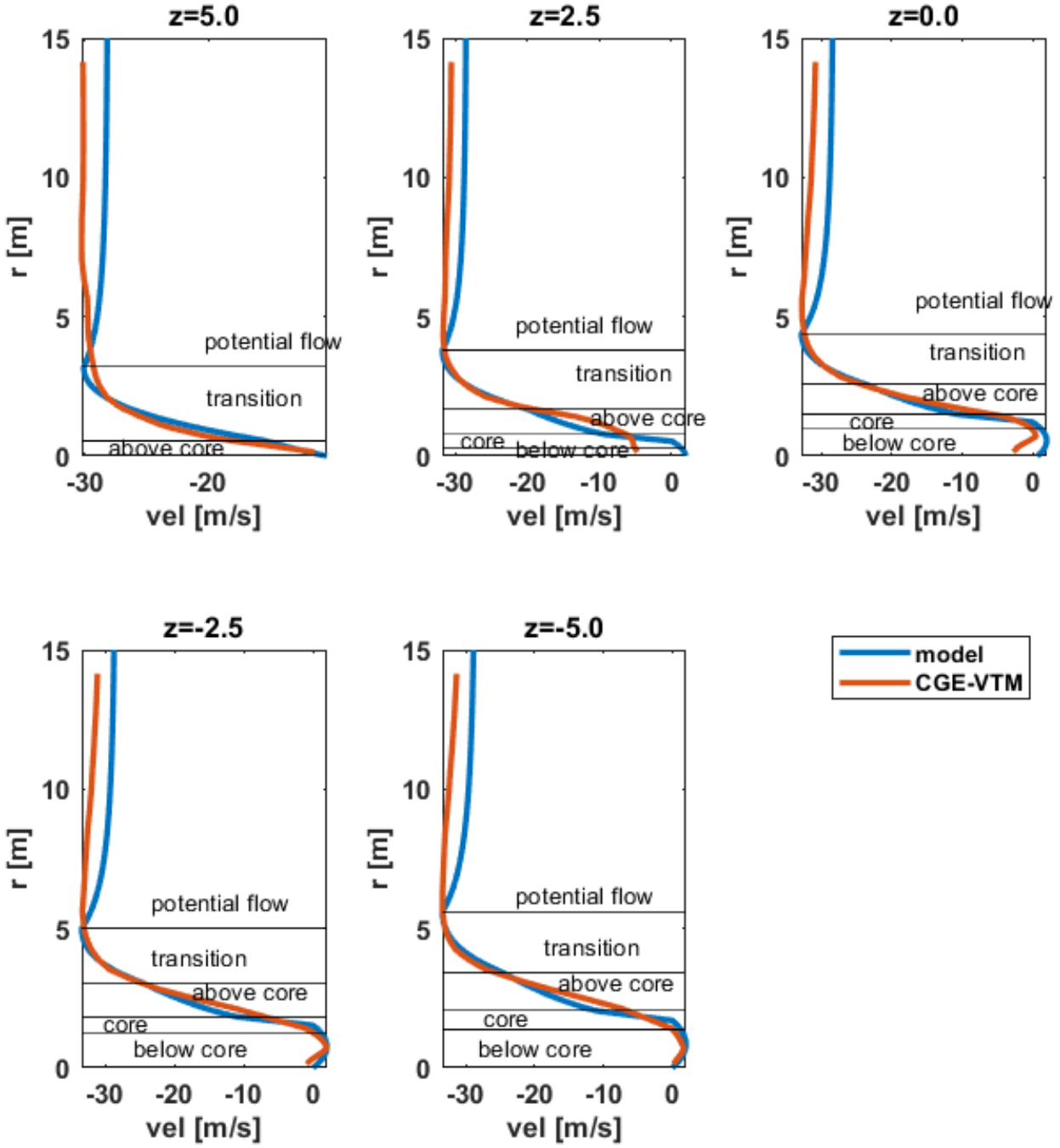

Figure 36: Longitudinal velocity profile along a 45° radial line from the corner of the cube at various span locations over the obstacle; CGE/VorTran-M data queried in 0.1 m incrments.

Next steps

As a precursor to full 3D reconstruction of the airwake using the 2D analytical fits developed thus far, work is currently underway to fit a vortex model along the 45° diagonal lines *aft* of the

obstacle, as illustrated by the blue dashed lines in Figure 37. Planes in which the 2D fits for the back and side flow separations were performed are highlighted as black dashed lines on the figure. Once models for the velocity profiles along the planes represented by the blue dashed lines are obtained, we plan to investigate the use of interpolation schemes to capture longitudinal velocity profile in the entire 3D space aft of the obstacle. Initial results obtained thus far (not included in this report) indicate that the ellipse-based and infinite vortex models used for the backflow separation can be applied to the along the diagonal planes with some tuning, further reinforcing the potential for parametrization of the model.

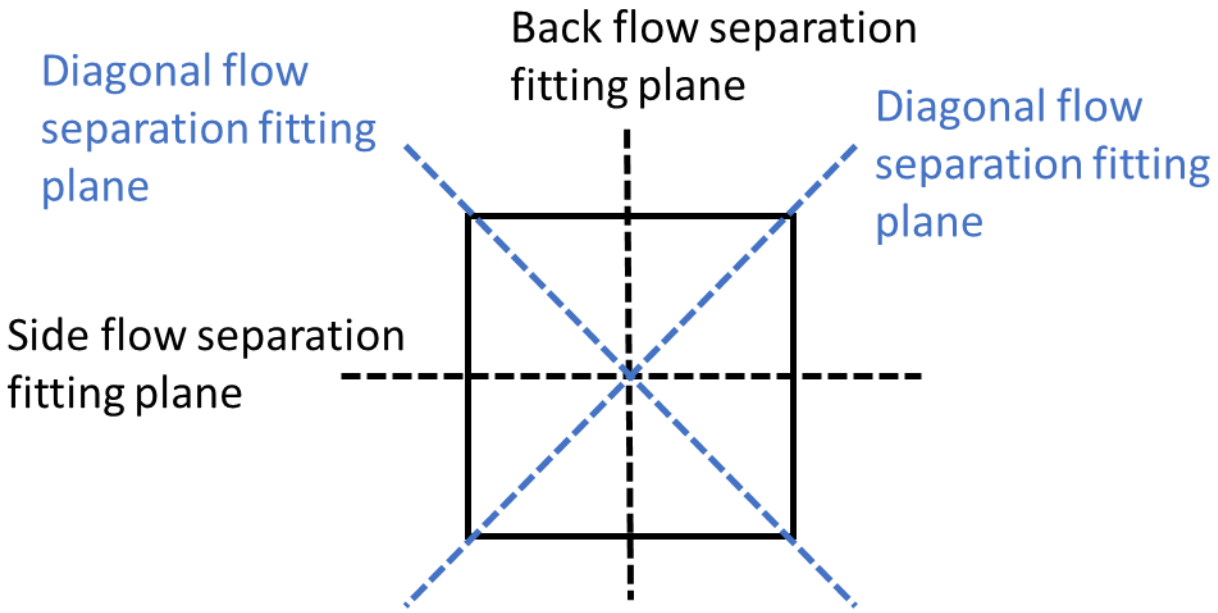

Figure 37: Illustration of planes (as dashed lines) where vortex model fitting is performed aft of the obstacle; black dashed lines represent planes along which model fitting has been performed while blue dashed lines represent planes we plan to consider; obstacle viewed from the back.

A similar interpolation based airwake reconstruction methodology will also be explored for the region over the obstacle, where we plan to perform to first expand the 2D infinite vortex models used for top and side surface separations to 3D by performing vortex fitting across the transverse planes indicated by the shaded regions in Figure 38. We then plan to perform velocity interpolations in the nonshaded region. If successful, we would be equipped analytical models capable of predicting time-averaged longitudinal velocity profiles over the cube. Models for the transverse and vertical velocity components would still have to be developed, in addition to accounting for airwake unsteadiness, potentially via a modal (mode shape) characterization of the flow features highlighted in Figure 6. Flow behavior upstream of the obstacle will need to be considered as well. Parametrization and scaling of the vortex-based models as a function of obstacle dimensions, wind speed and direction will also have to be investigated. We plan to explore these aspects further.

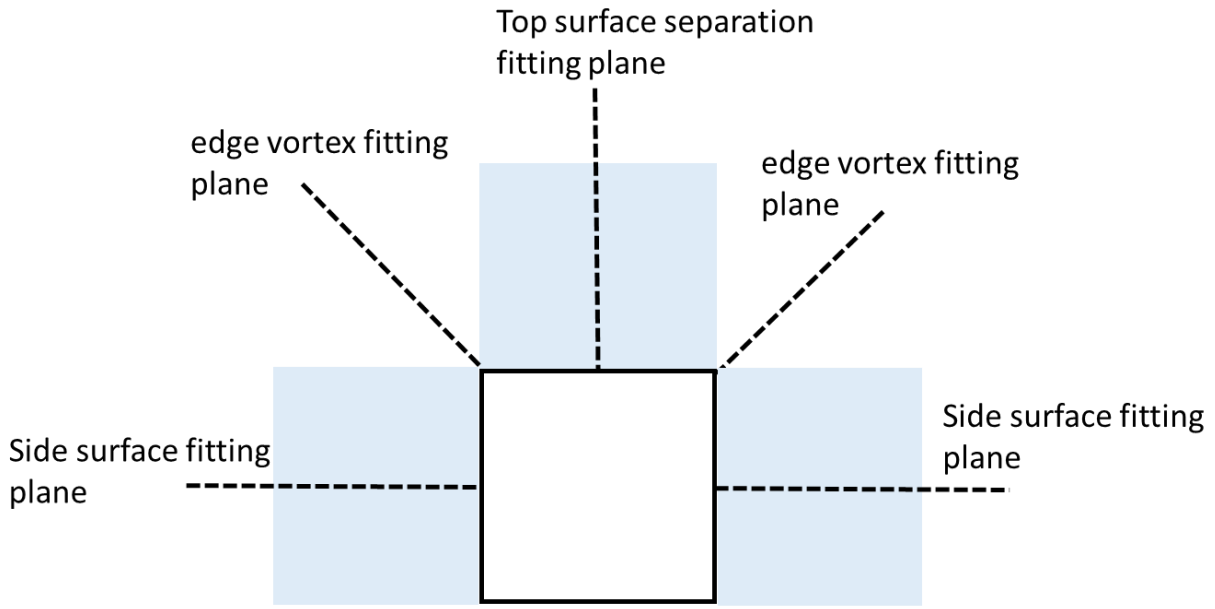

Figure 38: Illustration of planes (as dashed lines) where vortex model fitting is performed over the obstacle; shaded regions represent the transverse regions where we plan to perform additional model fitting; obstacle viewed from the back.

Plans for the Next Reporting Period

In the next reporting period, we will build upon the understanding of the types of flowfields experienced by naval aviators described above and continue to quantify the scales and nature of the relevant primary flow structures based on the ongoing CFD predictions. Development of representative "canonical" surrogate flowfields will continue. It is hoped that access to use NAVAIR/MFS' CASTLE simulation environment, the example helicopter model and the V-22 tiltrotor model for the duration of this project will be given.

References

1. Smith, M.J., A. Jones, A. Grubb, and J. Lefebvre. *Identification and Quantification of the Role of Turbulence in Aircraft/Ship Aerodynamics*. *ONR Annual Review*. 2020. Arlingon, VA.
2. Silva, M.J., D.A. Wachspress, D.P. Gaublomme, E.W. Hayden, T.S. Davis, and T. Fean. *The Role of Modeling & Simulation in the Mitigation of V-22 Tiltrotor Formation Flight Wake-Induced Roll-off*. *72nd Annual Forum of the American Helicopter Society*. 2016. West Palm Beach, FL.
3. Whitehouse, G.R. and R.E. Brown. *Modelling a Helicopter Rotor's Response to Encounters with Aircraft Wakes*. in *28th European Rotorcraft Forum*. 2002. Bristol, UK.
4. Whitehouse, G.R. and R.E. Brown. *Helicopter Rotor Response to Wake Encounters in Ground Effect*. in *59th Annual Forum of the American Helicopter Society*. 2003. Phoenix, AZ.

5. Whitehouse, G.R. and R.E. Brown, *Modelling the Mutual Distortions of Interacting Helicopter and Aircraft Wakes.* Journal of Aircraft, 2003. **Vol. 40**(No. 3): p. pp. 440-449.
6. Whitehouse, G.R. and R.E. Brown, *Modelling a Helicopter Rotor's Response to Wake Encounters.* The Aeronautical Journal, 2004. **Vol. 108**(No. 1079): p. pp. 15-26.
7. Whitehouse, G.R., *Helicopter Response to Vortex Encounters in the Near-Airfield Environment*, 2003, PhD Thesis, Department of Aeronautics Imperial College London.
8. ADS-33E-PRF. *Aeronautical Design Standard Performance Specification Handling Qualities Requirements for Military Rotorcraft*. in *US Army Aviation and Missile Command, Aviation Engineering Directorate*. 2000. Redstone Arsenal, Alabama.
9. Keller, J.D., G.R. Whitehouse, A.H. Boschitsch, J. Nadal, J. Jeffords, and M. Quire. *Computational Fluid Dynamics for Flight Simulator Ship Airwake Modeling*. in *Interservice/Industry Training, Simulation, and Education Conference (I/ITSEC) 2007*. 2007. Orlando, FL.
10. Whitehouse, G.R., A.H. Boschitsch, and P.V. Danilov. *Efficient Cartesian Grid CFD-Based Methods for Aeroelastic Analysis of Wind Turbines*. *2022 AIAA SciTech Forum*. 2022. San Diego, CA: AIAA-2022-1017.
11. Whitehouse, G.R., A.H. Boschitsch, and B.S. Silbaugh. *Development and Testing of a Low Cost CFD Based Analysis for Surface Mesh Interrogation & Refinement for Applied Aerodynamics Applications*. *56th AIAA Aerospace Sciences Meeting, AIAA SciTech Forum*. 2018. Kissimmee, FL: AIAA-2018-0541.
12. Sousa, J.M.M., *Turbulent Flow Around a Surface-Mounted Obstacle Using 2D-3C DPIV.* Experiments in Fluids, 2002. **Vol. 33**(No. 6): p. pp. 854-862.
13. Yakhot, A., H. Liu, and N. Nikitin, *Turbulent Flow Around a Wall-Mounted Cube: A Direct Numerical Simulation.* International Journal of Heat and Fluid Flow, 2006. **Vol. 27**(No. 6): p. pp. 994-1009.
14. Klotz, L., S. Goujon-Durand, J. Rokicki, and J.E. Wesfreid, *Experimental Investigation of Flow Behind a Cube for Moderate Reynolds Numbers.* Journal of Fluid Mechanics, 2014. **Vol. 750**: p. pp. 73–98.
15. Kim, K.C., H.S. Ji, and S.H. Seong, *Flow Structure around a 3-D Rectangular Prism in a Turbulent Boundary Layer.* Journal of Wind Engineering and Industrial Aerodynamics, 2003. **Vol. 91**(No. 5): p. pp. 653-669.
16. Banks, D. and R.N. Meroney, *A Model of Roof-Top Surface Pressures Produced by Conical Vortices: Model Development.* Wind and Structures, 2001. **Vol. 4**(No. 3): p. pp. 227–246.
17. Banks, D. and R.N. Meroney, *A Model of Roof-Top Surface Pressures Produced by Conical Vortices: Evaluation and Implications.* Wind and Structures, 2001. **Vol. 4**(No. 3): p. pp. 279–298.
18. Kozmar, H., *Surface Pressure on a Cubic Building Exerted by Conical Vortices.* Journal of Fluids and Structures, 2020. **Vol. 92**.
19. He, J. and C.C.S. Song, *A Numerical Study of Wind Flow around the TTU Building and the Roof Corner Vortex.* Journal of Wind Engineering and Industrial Aerodynamics, 1997. **Vols. 67-69**: p. pp. 547–558.
20. Liu, T., H. Zhang, and D. Xin, *Experimental Study on Mitigating Extreme Roof Suctions by Passive Vortex Generators.* Journal of Wind Engineering and Industrial Aerodynamics, 2021. **Vol. 219**.

21. Eaton, J.K. and J.P. Johnston, *Review of Research on Subsonic Turbulent-Flow Reattachment.* AIAA Journal, 1981. **Vol. 19**(No. 9): p. pp. 1093-1100.
22. Kim, J., S.J. Kline, and J.P. Johnston, *Investigation of a Reattaching Turbulent Shear Layer: Flow Over a Backward-Facing Step.* Journal of Fluid Engineering, 1980. **Vol. 102**(No. 3): p. pp. 302-308.
23. Eaton, J.K. and J.P. Johnston, *Low Frequency Unsteadiness of a Reattaching Turbulent Shear Layer*, in *Turbulent Shear Flows 3*. 1982, Springer. p. pp. 162-170.
24. Ma, X. and A. Schröder, *Analysis of Flapping Motion of Reattaching Shear Layer Behind a Two-Dimensional Backward-Facing Step.* Physics of Fluids, 2017. **Vol. 29**(No. 11).